Effects of two-phase inlet quality, mass velocity, flow orientation, and heating perimeter on flow boiling in a rectangular channel: Part 2 – CHF experimental results and model

Chirag R. Kharangate, Lucas E. O'Neill, Issam Mudawar *

Boiling and Two-Phase Flow Laboratory (BTPFL), School of Mechanical Engineering, Purdue University, 585 Purdue Mall, West Lafayette, IN 47907, USA

ABSTRACT

This study is the second part of a two-part study exploring flow boiling of FC-72 along a rectangular channel with either one wall or two opposite walls heated for saturated inlet conditions. While the first part examined flow boiling interfacial behavior, boiling curves, local and average heat transfer coefficients, and pressure drops, this part is focused entirely on CHF measurement, flow visualization and modeling. Both single-sided and double-sided heating configurations are tested in horizontal flow, vertical upflow, and vertical downflow. For low mass velocities, high speed video analysis shows gravity has a dominant influence on interfacial behavior, with single-sided top-wall heating yielding the lowest CHF values, and bottom-wall heating the highest. For both single-sided heating and double-sided heating, increasing mass velocity decreases the influence of orientation on CHF, with identical CHF values achieved at high mass velocities irrespective of orientation, and increasing inlet quality serves to decrease the mass velocity value required for inertia to completely overcome gravity effects. A separated flow model for two-phase inlet conditions is proposed to predict key flow variables necessary for CHF modeling. With a MAE $\leqslant$ 14%, this study proves that the combination of separated flow model and Interfacial Lift-off Model is highly effective at predicting CHF for saturated inlet conditions as it did in prior studies for subcooled inlet conditions.

1. Introduction

1.1. Boiling in thermal management

Advances in many modern electronics applications are benefiting from miniaturization technologies that have made possible enormous increases in functionality per device. But those same technologies have culminated in enormous increases in the amount of waste heat that must be removed from the device in order to maintain acceptable device temperatures. Gone is the era of simple air cooling using standard fin attachments, and even single-phase liquid cooling. Thermal design engineers are presently relying more than ever on two-phase thermal management solutions that capitalize on the enormous heat transfer coefficients possible with boiling. As discussed in [1], two key advantages of boiling over single-phase liquid cooling are (i) the ability to maintain much lower device temperatures for the same heat flux, and (ii) the relatively small changes in device temperature in response

to large fluctuation in the heat flux. It is important to emphasize that two-phase thermal management systems are not without shortcomings. In general, they tend be quite more complex and costlier than single-phase liquid cooling systems, which is why they are considered only where single-phase liquid cooling is deemed incapable of meeting the cooling demands of the application in question.

1.2. Use of body force versus inertia to achieve boiling performance

Of special interest to the present study is two-phase thermal management in future space missions, where high flow boiling and condensation heat transfer coefficients play a vital role in reducing size and weight of the thermal management hardware [2]. As shown in Fig. 1(a), these space missions are quite diverse in terms of gravitational environment, with gravities ranging from zero to Earth gravity, and Lunar and Martian gravities in between. Another extreme example is the high body force encountered during fast military aircraft maneuvers.

Body force can play positive or negative roles depending on both application and operating environment. In Earth gravity, the simplest and most economical boiling scheme is the pool

Nomenclature

A	cross-sectional area of flow channel		

Greek symbols

α	vapor void fraction
δ	mean thickness of vapor layer along heated walls
δ_a	mean thickness of vapor layer generated along heated wall H_a
δ_b	mean thickness of vapor layer generated along heated wall H_b
ε	liquid layer thickness
η	interfacial perturbation
η_0	amplitude of interfacial perturbation
λ_c	critical wavelength
μ	dynamic viscosity
ρ	density
ρ''	modified density
σ	surface tension
τ	shear stress
θ	flow orientation angle

A	cross-sectional area of flow channel
b	ratio of wetting front length to wavelength
c	wave speed
$C_{f,i}$	interfacial friction factor
c_i	imaginary component of wave speed
c_r	real component of wave speed
D	hydraulic diameter of channel
D_k	hydraulic diameter for phase k
f	friction factor
G	mass velocity
g_e	Earth gravity
H	height of flow channel's cross-section
H_a	heated wall a
H_b	heated wall b
h_{fg}	latent heat of vaporization
k	wave number
k_c	critical wave number
L	length
L_d	development length of flow channel
L_e	exit length of flow channel
L_h	heated length of flow channel
$\dot{m}$	mass flow rate
MAE	mean absolute error
N	number of data points
p	pressure
P_i	interfacial perimeter
p_{in}	pressure at inlet to heated portion of channel
P_w	wall perimeter
q_w''	wall heat flux
t	time
U	mean phase velocity
ΔU	phase velocity difference between heated wall vapor layer and liquid layer
W	width of flow channel's cross-section
x	flow quality
x_e	thermodynamic equilibrium quality
z	axial coordinate
z_0	axial coordinate where $U_g = U_f$
z^*	axial location for determining vapor layer thickness and critical wavelength in Interfacial Lift-off Model

Subscripts

a	vapor layer generated along heated wall H_a
b	vapor layer generated along heated wall H_b
c	critical; liquid layer in separated flow model
d	developing; middle vapor core in separated flow model
exp	experimental
f	saturated liquid; frictional
fc	saturated liquid in liquid layer c
g	saturated vapor
ga	saturated vapor generated along heated wall H_a
gb	saturated vapor generated along heated wall H_b
gd	saturated vapor in middle vapor core d
i	interfacial
in	inlet to heated portion of channel
k	phase k, $k = fc$, ga, gb or gd
m	wall identifier (a for heater H_a or b for heater H_b)
n	normal to heated wall
$pred$	predicted
w	wall; wetting front

thermosyphon [3], which capitalizes upon gravity, through buoyancy, to achieve passive fluid circulation as shown in Fig. 1(b). However, thermosyphons are associated with rather low critical heat flux (CHF) values, and often rely on additional surface augmentation techniques [3,4] to enhance boiling performance. Another method that relies on gravity to achieve passive fluid circulation and improve CHF is the pumpless loop concept [5] illustrated in Fig. 1(b). This system uses density differences between two parallel tubes, one adiabatic and the other to which the boiler is connected, to achieve the passive circulation. Another method which partially relies on gravity is the "semi-passive-circulation" falling-film cooling scheme [6,7]. However, gravity-driven schemes constitute low-end solutions when it comes to boiling heat transfer performance. In fact, most high-performance two-phase thermal management systems employ some form of flow boiling driven by a mechanical pump to circulate the coolant, and these schemes rely on flow inertia rather than buoyancy to achieve the desired cooling performance. During the past two decades, investigators have proposed and/or examined a variety of flow boiling schemes, including macro-channel [8], mini/micro-channel [9], jet impingement [10,11], and spray [12–14]. For example, high performance two-phase cooling of avionics onboard military aircraft can be achieved with high inertia combined jet/micro-channel flow, Fig. 1(c), that is designed to overcome the potentially detrimental influence of high body forces during fast military maneuvers [11]. Yet, a high artificially-induced body force can be highly effective at ameliorating CHF. Fig. 1(d) shows two cooling schemes that rely on high centrifugal force to pull vapor bubbles away from, and push bulk liquid toward the heated wall: flow boiling along a concave heated wall [15,16] and boiling enhanced by fluid rotation [17].

Despite decades of research to incorporate pool boiling in space applications, absence of gravity has been a key obstacle to maintaining stable nucleate boiling. In most of these studies, nucleating bubbles were observed to grow to enormous size along the heated, causing CHF to commence at very low heat fluxes [18]. In fact, it is now widely accepted that two-phase thermal management must incorporate a pumped loop that would remove the heat via flow boiling and deliver it to a condenser/radiator, where the heat is ultimately rejected by radiation to deep space [2]. In a pumped loop, flow inertia produces large drag and shear forces that remove vapor bubbles from the wall and sustain the liquid replenishment required to achieve high heat transfer coefficients and high CHF. While cooling performance may be ameliorated simply by
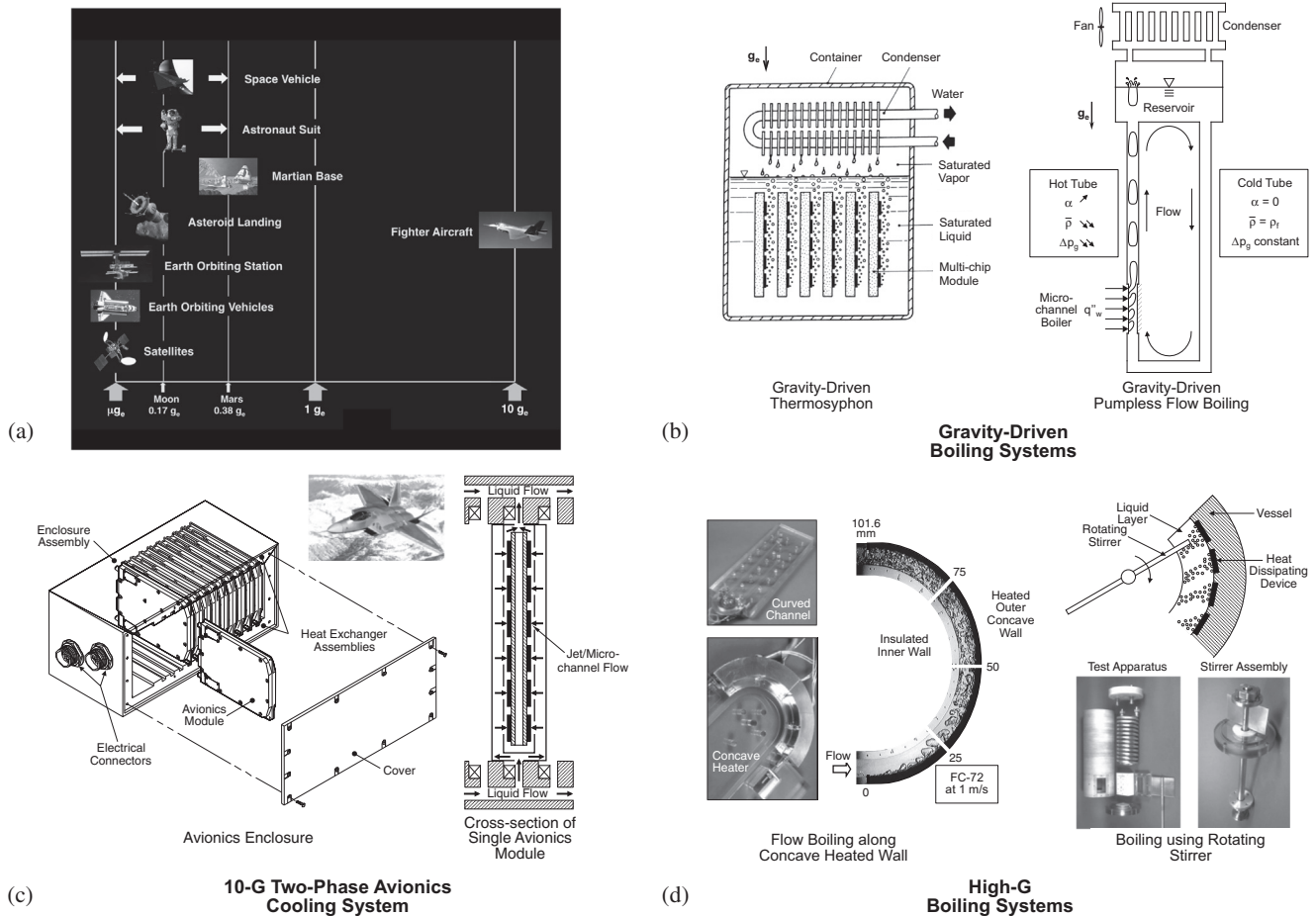
Fig. 1. (a) Space systems demanding predictive models of the effects of gravity on two-phase flow and heat transfer, and examples of different strategies for tackling gravity effects in boiling systems: (b) using buoyancy in passive cooling systems at one g_e [1,3], (c) negating body force effects induced during military aircraft maneuvers using high inertia jet/micro-channel flow [11], and (d) using centrifugal force to produce very high body force [15–17].

increasing the coolant's flow rate, it is equally desired to use minimal pumping power to conserve limited power resources onboard the space vehicle. Therefore, the strategy adopted in space applications is use the minimum flow rate (*i.e.,* minimum pumping power) required to achieve the desired cooling performance.

1.3. Flow boiling critical heat flux (CHF)

Critical heat flux (CHF) is arguably the most important design parameter for systems utilizing flow boiling to cool a device. This is especially the case for applications involving heat-flux-controlled heat input, where CHF can trigger a rapid unsteady rise in surface temperature, often culminating in damaging, overheating or burnout of the device. There are two main types of CHF: dryout and Departure from Nucleate Boiling (DNB). Dryout is typically encountered in channels where the coolant is supplied with low subcooling and at low mass velocity, and subjected to low wall heat flux. Assuming the channel in sufficiently long, these conditions lead to gradual vapor buildup along the channel, spanning single-phase liquid, bubbly, slug and annular flow regimes, and CHF is associated with dryout of the annular film. Given the combination of low wall heat flux and axial conduction in the wall, dryout is a relatively mild form of CHF. DNB, on the other hand, is generally encountered when the coolant is supplied to the channel in highly subcooled state and at high mass velocity, and subjected to high wall heat flux. Here, CHF is triggered along the channel wall due to localized formation of a coalescent vapor blanket, even at axial locations containing abundant liquid flow. In other words, it

is the result of a mechanism that precludes liquid access to the heated wall, the outcome of which is a dangerous escalation in the wall temperature and high probability of physical damage. Therefore, there is a need to accurately predict CHF as a function of the coolant's mass velocity, inlet quality and thermophysical properties, and the channel's geometry. This would allow thermal engineers to select operating conditions to yield a wall heat flux safely below CHF. Hereafter in the present study, CHF is used to refer to the more dangerous DNB mechanism.

1.4. Flow boiling CHF mechanisms and models

CHF is a very complex phenomenon. And failure to identify a single mechanism or construct a universal model for CHF has driven most researchers to pursue empirical CHF formulations [19–22]. While correlations are quite useful, and have served as basis for design of flow boiling systems for decades, their validity is limited to the specific fluids and ranges of operating conditions of the databases upon which these correlations are based.

Only a few models have been proposed for flow boiling CHF, and are based on four competing mechanisms [18]:

1.4.1. Boundary layer separation model

Proposed by Kutateladze and Leont've [23], this model's formulation is based on analogy between vapor production from a heated wall in flow boiling, and gas injection from a permeable wall into a turbulent boundary layer. In the same manner the turbulent boundary layer separates when the gas injection velocity exceeds

a threshold value, CHF is believed to occur when the rate of vapor production increases to a level that greatly decreases near-wall liquid velocity, reducing the bulk liquid's ability to replenish the heated wall.

1.4.2. Bubble crowding model

This model is based on the premise that a key precursor to CHF is formation of a bubbly boundary layer containing closely packed oblong vapor bubbles. This layer resists the radial flow of bulk liquid to the wall resulting from liquid turbulent fluctuations. Weisman and Pei [24] suggested CHF commences when the void fraction in the bubbly layer reaches a critical value.

1.4.3. Sublayer dryout model

Originally proposed by Lee and Mudawar [25] and later adopted by other investigators [26], this model is based on the observation that flow boiling CHF is preceded by formation of oblong bubbles along the heated wall, each trapping a thin liquid film – sublayer – between the bubble and the wall. The sublayer is replenished by bulk liquid, and CHF is postulated to occur when the liquid replenishment falls short of compensating for the rate of evaporation of the sublayer's liquid.

1.4.4. Interfacial Lift-off Model

This model was proposed by Galloway and Mudawar [27,28] based on extensive high-speed video records of interfacial features just before and during CHF. These records show that, at wall heat fluxes slightly below CHF, vapor coalesces into a wavy layer that propagates along the heated wall, while liquid replenishment is available only within the wave troughs – wetting fronts – aided by radial pressure induced by curvature of liquid streamlines along the wavy layer's interface. CHF is postulated to occur when the intense momentum of vapor generated in the wetting fronts exceeds the pressure force, which causes the wavy vapor layer's interface in the wetting fronts to lift away from the wall, extinguishing liquid access to the wall. In recent years, several studies were conducted at the Purdue University Boling and Two-Phase Flow Laboratory (PU-BTPFL) [15–17,29–36] that corroborate the effectiveness of *Interfacial Lift-off Model* in predicting CHF for short and long heated walls, flat and curved walls, horizontal, vertical, and inclined channels, and flow boiling in both Earth gravity and microgravity.

1.5. Effects of body force on CHF

As indicated above, body force has a significant impact on flow boiling CHF where flow inertia is weak, *i.e.*, at low mass velocities. The effects of body force are felt in the form of product of gravity and density difference between liquid and vapor. In Earth gravity, the impact of body force is complicated by flow orientation, which yields two components of body force, one perpendicular to the heated wall, and the other parallel to (or opposite) the flow direction. These effects are best reflected in experiments involving a rectangular flow channel with one heated wall. Zhang et al. [34,35] conducted such experiments using FC-72 as working fluid to map the complex interfacial patterns associated with different mass velocities and flow orientations from horizontal with the heated wall upward facing ($\theta = 0°$) and increasing in 45° increments. At low mass velocities, the influence of orientation was very profound. For upward-facing heated wall orientations ($\theta = 315°$, 0° and 45°), the component of body force perpendicular to the heated wall was observed to aid vapor removal from, and liquid replenishment of the heated wall, yielding a positive impact on CHF. Conversely, downward-facing heated wall orientations ($\theta = 135°$, 180°, and 225°) caused stratification of vapor along the heated wall, leading to low CHF values. The component of gravity parallel

to (or opposite) the flow direction also played an important role. They observed upflow and near upflow orientations ($\theta = 45°$, 90°, and 135°) cause this component of body force to assist vapor purging along the direction of fluid flow, while downflow and near downflow orientations ($\theta = 225°$, 270°, and 315°) cause the same component of body force to resist vapor removal, even causing vapor backflow toward the inlet of the flow channel. Overall, the experiments of Zhang et al. proved CHF at low mass velocities can be ameliorated with combinations of upflow and upwards-facing heated wall orientations, and compromised with combinations of downflow and downward-facing orientations. However, they also proved that flow orientation becomes inconsequential at high mass velocities, resulting is fairly equal CHF values, as high inertia negates altogether the influence of body force. The minimum value of mass velocity at which body force effects are negated is especially important to reduced gravity space applications for two reasons: (1) it renders CHF data, correlations and models developed in Earth gravity applicable to space system design, and (2) it requires the least pumping power to achieve the same goal. Determining this minimum value is of special importance to the present study. Zhang et al. [36] later extended their findings to reduced gravity conditions by conducting experiments in parabolic flight. These experiments confirmed the Interfacial Lift-off Model [27,28] for flow boiling CHF at all mass velocities in microgravity.

These experiments by Zhang et al. where conducted with slightly subcooled inlet conditions ($x_{e,in} \simeq 0$). However, the effects of body force can be complicated further with saturated ($x_{e,in} > 0$) [37] or highly subcooled ($x_{e,in} \ll 0$) [38] inlet conditions, which can have a strong influence on vapor void fraction and therefore both flow inertia and liquid availability along the channel. Another highly complicating factor is the use of two opposite heated walls. Here, the same body force component that aides vapor removal from, and liquid replenishment of one heated wall will have the opposite influence on the opposite heated wall [38,39]. Despite several studies to address these complicating factors, no studies have been performed to address simultaneously the effects of mass velocity, inlet quality, flow orientation, and both single-sided and double-sided heating. Addressing all these parameters is precisely the goal of the present study.
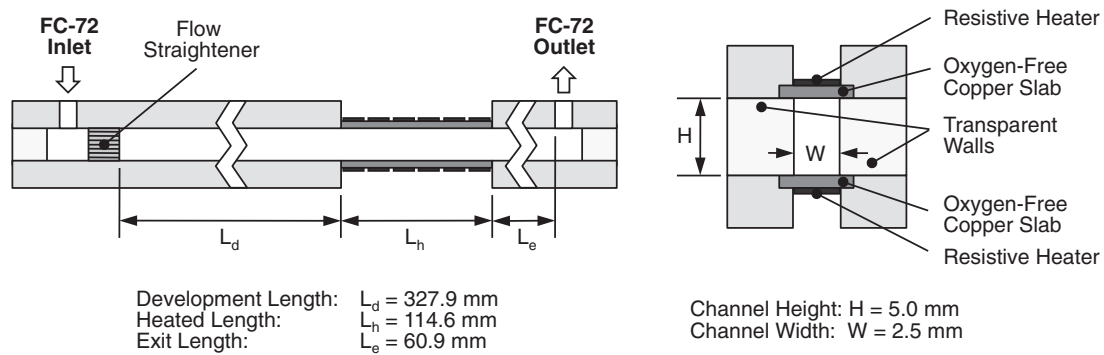
1.6. Objective of study

This two-part study is a comprehensive investigation of flow boiling and CHF in inclined channels with single-sided and double-sided heating and over broad ranges of mass velocity and inlet quality. This study is part of a NASA project whose ultimate goal is to develop the Flow Boiling and Condensation Experiment (FBCE) for the International Space Station (ISS). The first part of the study [40] examined flow boiling interfacial behavior, boiling curves, local and average heat transfer coefficients, and pressure drop. This part of the study will be focused entirely on the combined influences of mass velocity, inlet quality, flow orientation, and both single-sided and double-sided heating on flow boiling CHF, and on CHF modeling.
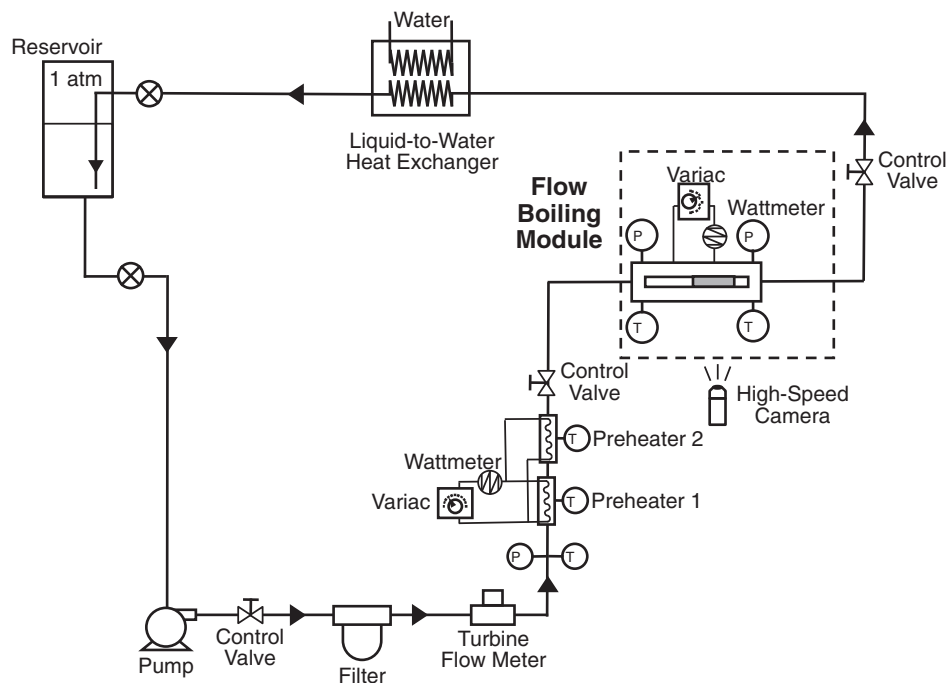
2. Experimental methods

2.1. Flow boiling module and heated wall construction and instrumentation

Fig. 2(a) shows a schematic of the flow boiling module that is used to measure CHF. The flow channel in this module has a rectangular cross-section with a width of $W = 2.5$ mm and height of $H = 5.0$ mm. It is also comprised of three axial regions: a

FC-72 Inlet Flow Straightener **FC-72 Outlet**

Development Length: L_d = 327.9 mm
Heated Length: L_h = 114.6 mm
Exit Length: L_e = 60.9 mm

Resistive Heater
Oxygen-Free Copper Slab
Transparent Walls
Oxygen-Free Copper Slab
Resistive Heater

Channel Height: H = 5.0 mm
Channel Width: W = 2.5 mm

(a)

(b)

Fig. 2. (a) Schematic of flow boiling module and key dimensions. (b) Two-phase flow loop.

hydrodynamic development length of L_d = 327.9 mm, a heated length of L_h = 114.6 mm, and an exit length of L_e = 60.9 mm.

The heated section contains two opposite copper slabs, each is heated by an array of thick-film resistors, with the other two side-walls made from transparent polycarbonate plastic (Lexan) to facilitate optical access to the boiling flow. The heated walls are configured to be powered either individually to achieve single-sided heating, or simultaneously for double-sided heating.

Zhang et al. [36] showed that a minimum copper wall thickness of 0.4 mm is required to measure 'asymptotic' CHF values representative of practical engineering surfaces, while smaller thicknesses yield smaller CHF values that are wall-thickness dependent. The 0.4-mm thickness therefore constitutes a lower bound for the copper walls. On the other hand, much larger thicknesses are also undesirable since they increase the time required to reach steady state between power increments, as well as contribute significant axial conduction along the heated wall during

CHF detection. Therefore, a copper wall thickness of 1.04 mm is used in the present study.

Heated wall temperatures are measured by a series of seven type-E thermocouples that are soldered into shallow grooves in each copper slab. A second series of thermocouples at the same axial locations, but offset from the copper slab's centerline, is used to cut off power input to the heated wall(s) during CHF detection with the aid of a solid-state relay should the temperature measured by any thermocouple in the same series exceed 130 °C.

Two-phase interfacial features in the heated portion of the flow channel are examined with the aid of a high speed camera at a rate of 2000 frames per second for a period of 1 s, with each image capturing the entire heated length with 2040 × 156 resolution. At CHF, the recording period is increased to 4 s, capturing a total of 8000 frames to better track the evolution of the CHF transient. Lighting is provided by four LEDs, with a diffuser placed between the LEDs and flow boiling module.

2.2. Two-phase flow loop and operating conditions

FC-72 is supplied to the inlet of the flow boiling module in saturated state (with $x_{e,in} > 0$) at the desired pressure and mass velocity using the flow loop depicted schematically in Fig. 2(b). The fluid is pumped in liquid state from a reservoir into a filter, turbine flow meter, and two electric preheaters where the liquid is converted to a saturated mixture at the desired $x_{e,in}$. The fluid incurs additional phase change along the flow boiling module, and is returned to liquid state by flowing through a water-cooled heat exchanger, before returning to the reservoir.

The operating conditions for the study are as follows: G = 183.5–2030.3 kg/m²s, inlet pressure of p_{in} = 109.7–191.8 kPa (15.9– 27.8 psi), and inlet thermodynamic equilibrium quality of $x_{e,in}$ = 0.00–0.69. The fluid pressure and temperature are measured by STS absolute pressure transducers and type-E thermocouples, respectively, at several locations along the flow loop as well as the inlet and outlet of the flow boiling module. The accuracies of the measurements sensors are ±0.05%, ±0.5 °C, and ±0.1% for the pressure transducers, thermocouples, and turbine flow meter, respectively. The wall heat flux and CHF are measured with an accuracy of ±0.5 W.

Additional details concerning the experimental methods are provided in the first part of the study [40].

3. Experimental results

3.1. Flow visualization of CHF

Fig. 3(a) and (b) show flow orientations relative to Earth gravity that are examined in this study for single-sided and double-sided heating. The flow in Fig. 3(a) is shown for all orientations entering from the center and radiating outwards. Three orientations are examined: horizontal flow (θ = 0° and 180°), vertical upflow (θ = 90°), and vertical downflow (θ = 270°), with each including single-sided and double-sided heating. In horizontal flow, single-sided heating involves two distinct heating configurations, upward-facing (θ = 0°) and downward-facing (θ = 180°). For double-sided heating, both upward-facing or downward-facing heaters are activated simultaneously, rendering the two horizontal configurations of θ = 0° and θ = 180° identical due to symmetry. Fig. 3(b) shows all configurations discussed in this study, including single-sided and double-sided heating.

Fig. 4(a) shows flow visualization results for horizontal flow with single-sided and double-sided heating corresponding to one heat flux below CHF and during CHF. For G = 198.4–217.9 kg/m²s and inlet qualities of $x_{e,in}$ = 0.00–0.02 and 0.07–0.10, top wall heating, and top and bottom wall heating, show wetting fronts being lifted away from heated wall(s) during CHF. For bottom wall
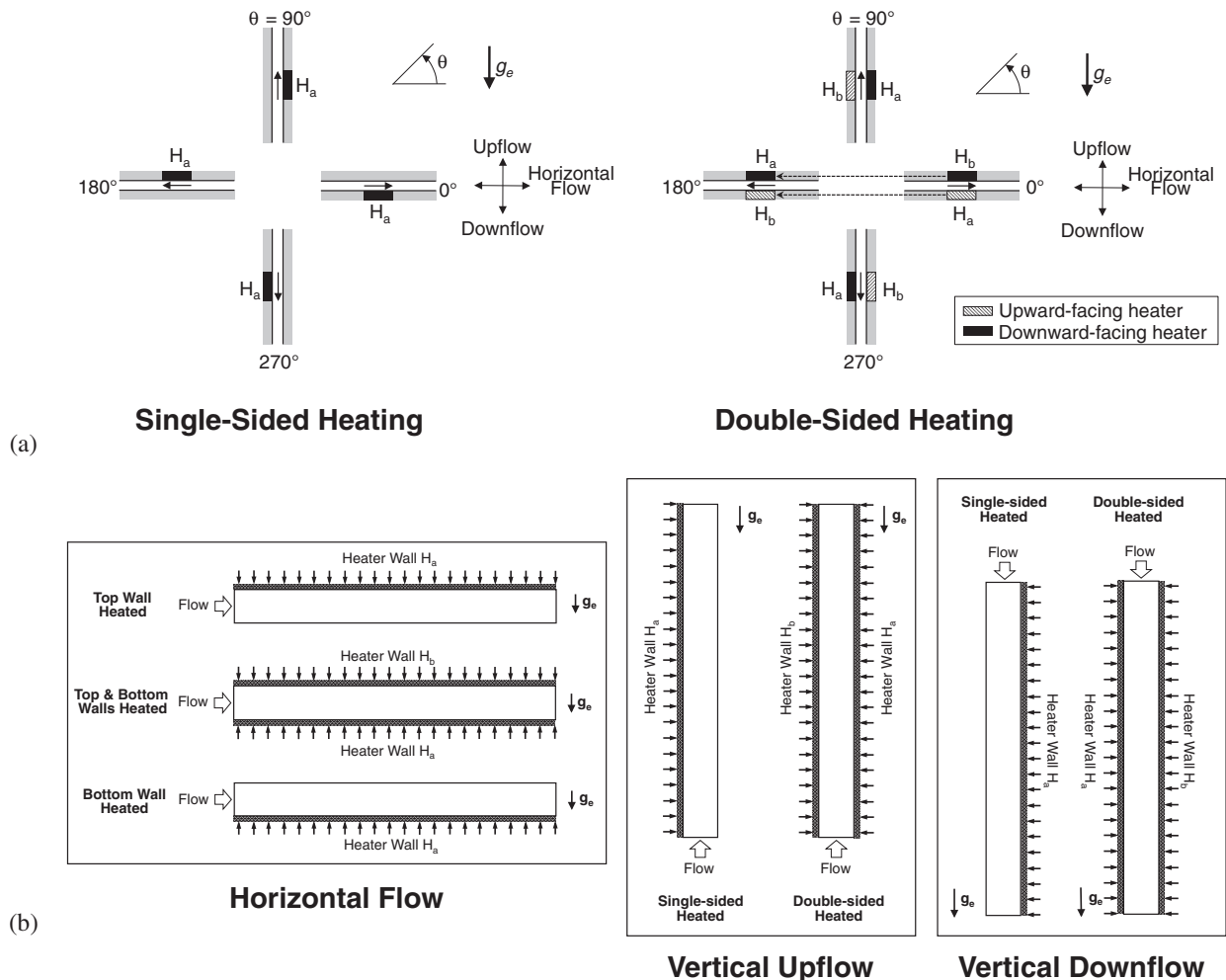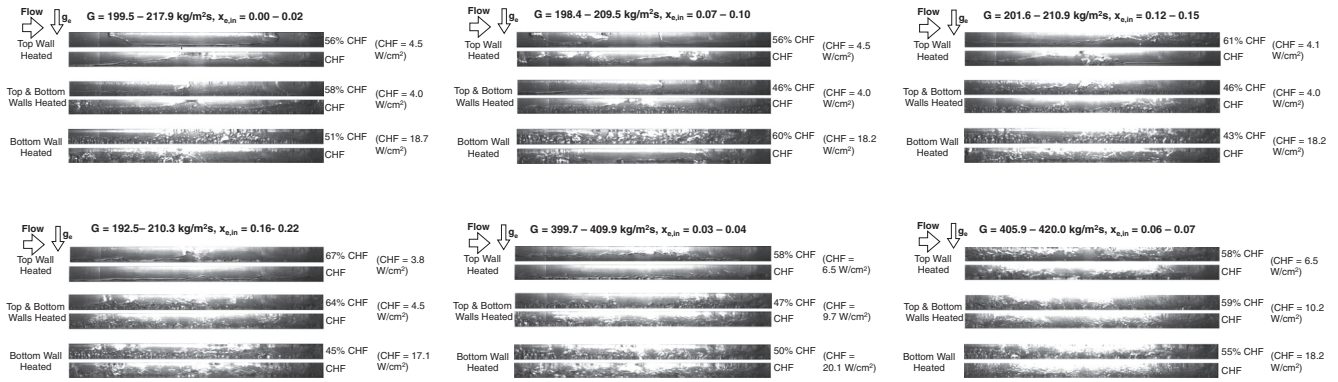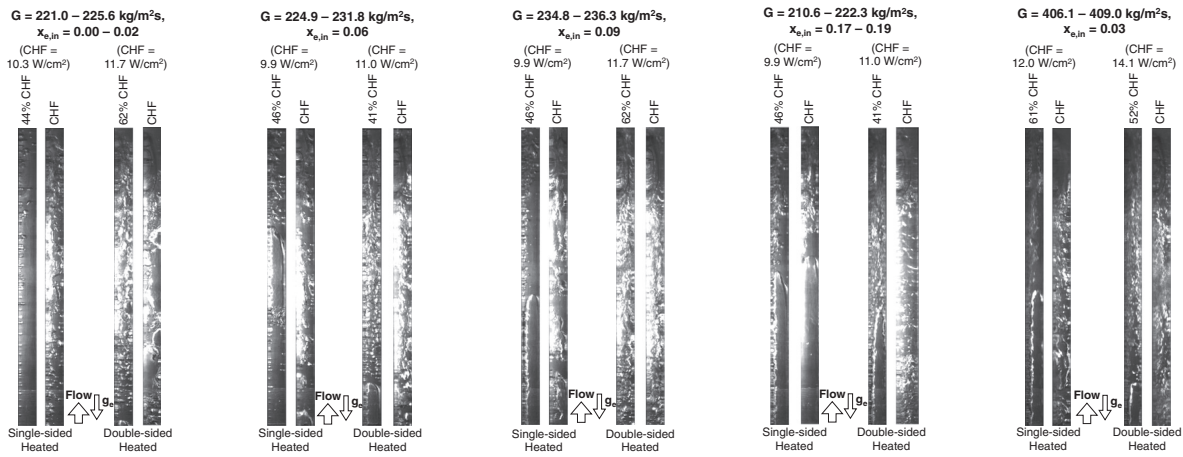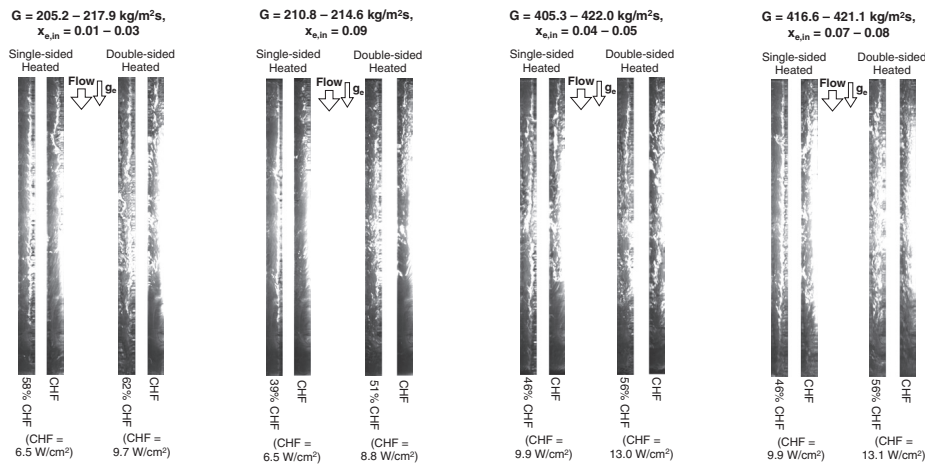

Fig. 3. (a) Flow orientation and heater nomenclature for single-sided heating and double-sided heating in Earth gravity. (b) Heated wall nomenclature for each orientation with single-sided and double-sided heating.

Fig. 4. Variations of interfacial behavior before and during CHF for (a) horizontal flow configurations, (b) vertical upflow configurations, and (c) vertical downflow configurations.

heating, it is difficult to assess the transient CHF behavior close to the heated wall because of mixing of a large volume of vapor generated along the heated wall with the incoming vapor–liquid mixture. Increasing the inlet quality to $x_{e,in} = 0.12$–0.15 and 0.16–0.22 is shown increasing the vapor's void fraction along the heated portion of the channel while preserving interfacial behavior near the walls. As the mass velocity is increased to $G = 399.7$–420.0 kg/m² s, a thick stratified vapor layer is captured along the top wall for top wall heating, and top and bottom wall heating, which

appears to trigger CHF for this mass velocity and both $x_{e,in} = 0.03$–0.04 and 0.06–0.07. For bottom wall heating, the flow at $G = 399.7$–420.0 kg/m² s is highly turbulent, with the incoming vapor–liquid mixture combining with the vapor generated along the bottom wall, rendering identification of near-wall interfacial behavior quite elusive.

Fig. 4(b) shows flow visualization results for vertical upflow with single-sided and double-sided heating. At $G = 221.0$–225.6 kg/m² s and $x_{e,in} = 0.00$–0.02, very little vapor is

seen entering the channel. At CHF, a thick vapor layer is seen engulfing a significant portion of the heated wall for both single-sided and double-sided heating. As the inlet quality is increased to $x_{e,in} = 0.06$ for a similar mass velocity, slug flow is seen entering the channel, which is combined with the vapor generated along the heated wall(s). A further increase in inlet quality to $x_{e,in} = 0.09$ is shown increasing void fraction both at the inlet and along the heated wall(s) while preserving interfacial behavior in the near-wall region. Increasing the mass velocity to $G = 406.1$–409.0 kg/m² s with an inlet quality of $x_{e,in} = 0.03$ is shown producing interfacial behavior similar to that for the lower mass velocity.

Fig. 4(c) shows flow visualization results for vertical downflow with single-sided and double-sided heating. At mass velocities of $G = 205.2$–217.9 and 405.3–422.0 kg/m² s, the entire channel is seen engulfed with a turbulent vapor–liquid mixture comprised of incoming vapor mixed with the vapor generated along the heated wall(s), making identification of near-wall interfacial behavior quite difficult.

3.2. Experimental CHF trends

3.2.1. Orientation effects on CHF

Fig. 5(a)–(d) show polar plots of CHF for single-sided heating over a range of mass velocities at inlet qualities of $x_{e,in} = 0.00$–0.05, 0.07–0.15, 0.19–0.25, and 0.62–0.69, respectively. For the lowest inlet quality range of $x_{e,in} = 0.00$–0.05, Fig. 5(a) shows CHF values for the lowest mass velocity of $G = 197.1$–226.5 kg/m² s

are lowest for top-wall heating ($\theta = 180°$) due to vapor stratification along the heated wall, while vertical uplow ($\theta = 90°$) and vertical downflow ($\theta = 270°$) show better performances, a trend shared with heat transfer coefficients and pressure drops in the first part of this study [40]. CHF values for vertical upflow are slightly higher than those for vertical downflow. This is due to the upflow orientation assisting vapor removal; the opposite is true for vertical downflow. However, CHF differences between the upflow and downflow orientations are not significant even at low mass velocities because the saturated inlet conditions greatly increase the magnitude of inertial forces of incoming fluid in comparison with gravity. Horizontal flow with bottom-wall heating ($\theta = 0°$) shows the best performance, which can be attributed to strong buoyancy effects aiding vapor removal from, and liquid replenishment of the heated wall. For the same low quality range of $x_{e,in} = 0.02$, Fig. 5(a) shows increasing mass velocity to $G = 1214.3$–1252.3 kg/m²s completely negates the influence of orientation and therefore body force. Fig. 5(b)–(d) show the mass velocities at which the effects of orientation on CHF are completely negated at $x_{e,in} = 0.07$–0.15, 0.19–0.25, and 0.62–0.69 are $G = 784.4$–815.5, 794.4–800.8, and 400.4–412.2 kg/m² s, respectively. Therefore, increasing inlet quality decreases the mass velocity required for inertia to overcome gravity effects. This can be explained by higher $x_{e,in}$ increasing liquid and vapor velocities and, therefore, flow inertia upstream of the heated portion of the channel.

Fig. 6(a)–(d) show polar plots of CHF for double-sided heating over a range of mass velocities at inlet qualities of
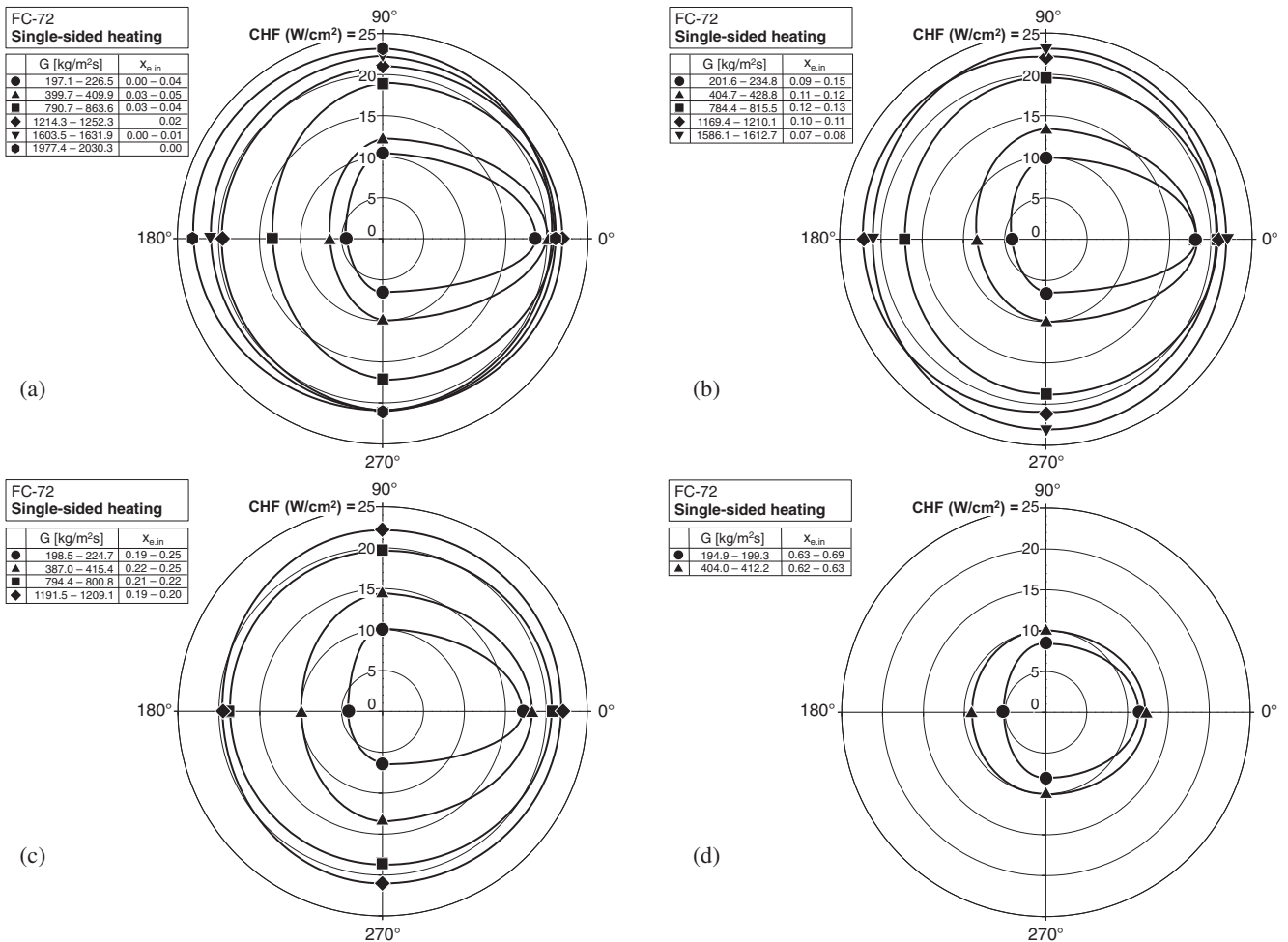

Fig. 5. Polar plots showing variations of CHF with orientation relative to Earth gravity for single-sided heating and different mass velocities with (a) $x_{e,in} = 0.00$–0.05, (b) $x_{e,in} = 0.07$–0.15, (c) $x_{e,in} = 0.19$–0.25, and (d) $x_{e,in} = 0.62$–0.69.
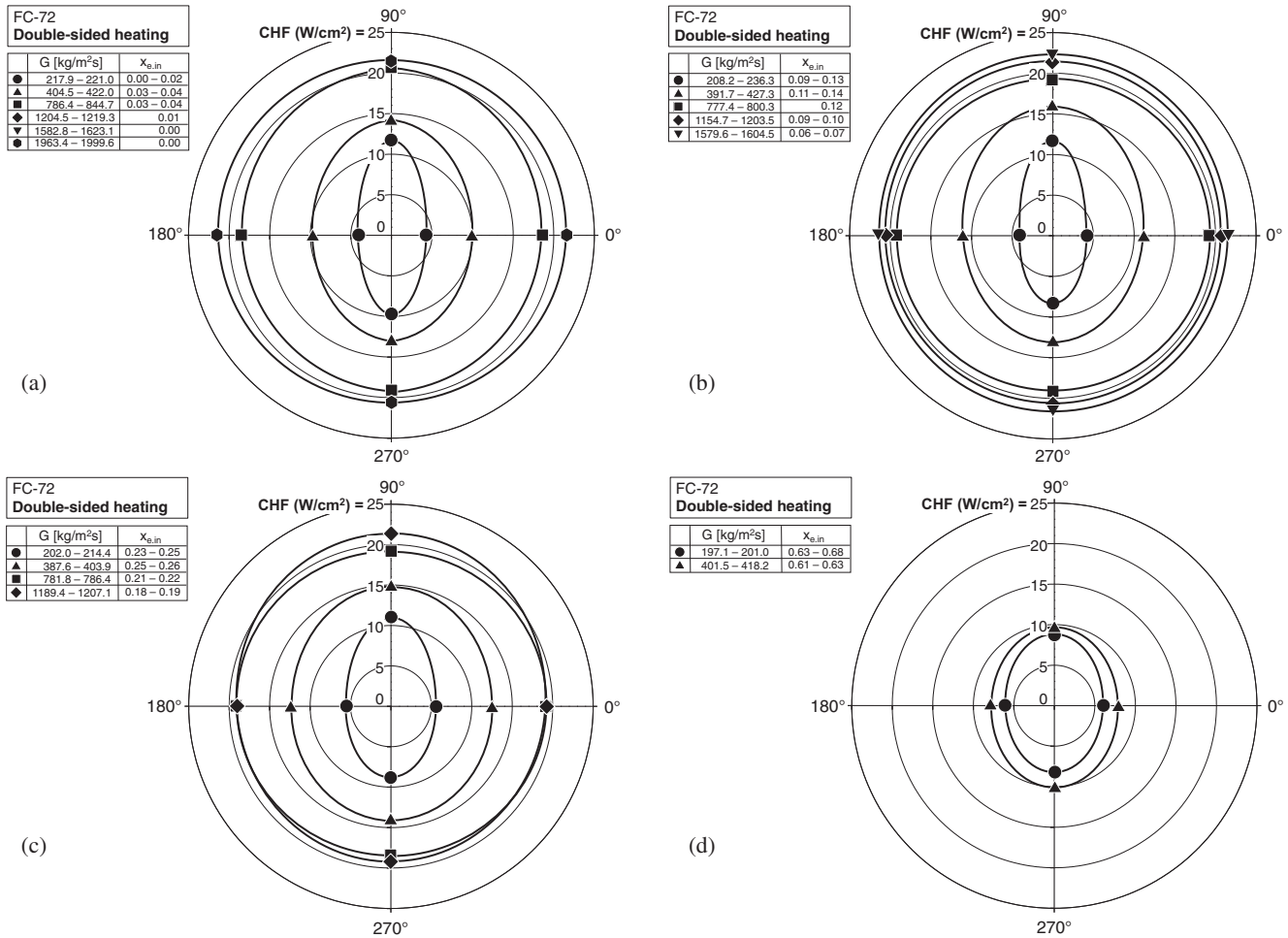
Fig. 6. Polar plots showing variations of CHF with orientation relative to Earth gravity for double-sided heating and different mass velocities for (a) $x_{e,in}$ = 0.00–0.04, (b) $x_{e,in}$ = 0.06–0.14, (c) $x_{e,in}$ = 0.18–0.26, and (d) $x_{e,in}$ = 0.61–0.68.

$x_{e,in}$ = 0.00–0.04, 0.06–0.14, 0.18–0.26, and 0.61–0.68, respectively. Notice that, because of double-sided heating, CHF values are symmetrical around the vertical axis. For example, horizontal flows at θ = 0° and 180° both include top-wall and bottom-wall heating, rendering the two orientations identical. For $x_{e,in}$ = 0.00–0.02 and G = 217.9–221.0 kg/m² s, Fig. 6(a) shows vertical upflow (θ = 90°) and vertical downflow (θ = 270°) greatly outperforming the horizontal orientations (θ = 0° and 180°). The relatively inferior performances of the horizontal orientations can be explained by their reliance on both top-wall and bottom-wall heating, which compromises their overall performance by vapor stratification along the top wall. The mass velocities at which the effects of orientation on CHF are fully negated for $x_{e,in}$ = 0.00–0.04, 0.06–0.14, 0.18–0.26, and 0.61–0.68 are G = 786.4–844.5, 777.4–800.3, 387.6–403.9, and 401.5–418.2 kg/m² s, respectively. Like the trend for single-sided heating, Fig. 5(a)–(d), the results in Fig. 6(a)–(d) for double-sided heating show increasing $x_{e,in}$ decreases the mass velocity required for inertia to overcome gravity. Here, again, the higher $x_{e,in}$ is believed to increase the velocities of both vapor and liquid at the inlet, which increases flow inertia upstream of the heated portion of the channel. But the main difference between single-sided and double-sided results is the increased flow acceleration and inertia with double sided heating, where vapor is generated along both walls. This difference is reflected in a lower mass velocity range of G = 786.4–844.7 kg/m² s corresponding to full negation of orientation effects at $x_{e,in}$ = 0.00–0.04, Fig. 6(a), compared to G = 1214.3–1252.3 kg/m² s for $x_{e,in}$ = 0.02, Fig. 5(a).

3.2.2. Inlet quality effects on CHF

Fig. 7(a)–(c) show variations of CHF for double-sided heating with $x_{e,in}$ over a range of mass velocities for horizontal flow (θ = 0 and 180°), vertical upflow (θ = 90°) and vertical downflow (θ = 270°), respectively. For all three orientations, CHF for a fixed $x_{e,in}$ is shown increasing monotonically with increasing G. A very interesting trend for all three orientations at low mass velocities is CHF first increases with increasing $x_{e,in}$, reaches peak value, and decreases thereafter. The initial increase can be explained by the increased $x_{e,in}$ increasing inlet velocities of both the liquid and vapor. Downstream from the peak value, the benefits of those increases are counterbalanced by an appreciable increase in vapor volume and corresponding scarcity of liquid along the channel. For horizontal flow (θ = 0 and 180°), Fig. 7(a) shows peak CHF values for G = 183.5–217.9 and 387.6–417.7 kg/m² s are achieved around $x_{e,in}$ = 0.35. The inlet quality corresponding to peak value decreases to around $x_{e,in}$ = 0.15 for 777.4–796.9 kg/m² s, and $x_{e,in}$ = 0 for all higher mass velocities. For vertical upflow (θ = 90°), Fig. 7(b) shows CHF variations with $x_{e,in}$ for different mass velocities are less pronounced than those for horizontal flow. It is difficult to assign a value for $x_{e,in}$ corresponding to peak CHF for the lowest mass velocity range of G = 197.1–236.3 kg/m² s. However, peak CHF is achieved around $x_{e,in}$ = 0.15 for G = 391.7–409.0 kg/m² s, and close to $x_{e,in}$ = 0 for G = 786.4–809.1 kg/m² s, and CHF variations with $x_{e,in}$ are similar to those for vertical upflow, Fig. 7(c), with some variations in $x_{e,in}$ values corresponding to peak CHF.
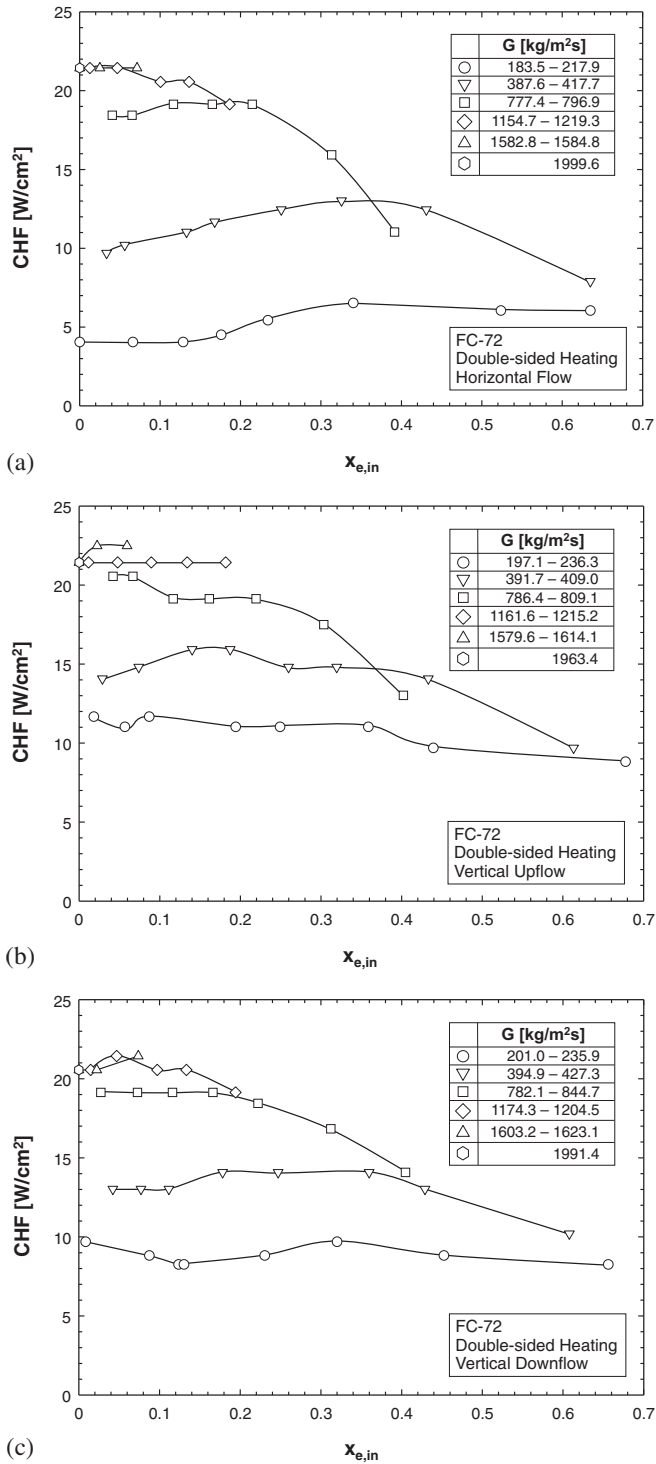
Fig. 7. Variations of CHF for double-sided heating with inlet quality for different mass velocities in (a) horizontal flow, (b) vertical upflow, and (c) vertical downflow.

4. CHF model

4.1. Separated flow model

A separated flow model is constructed to predict key flow variables necessary for development of a mechanistic CHF model. For the saturated inlet conditions ($x_{e,in} > 0$) of the present study, the FC-72 is supplied to the heated portion of the channel as a vapor–liquid mixture. Excepting horizontal flows at low mass velocities, where the inlet mixture is stratified, the fluid for most operating conditions and orientations enters the channel fully separated with a liquid layer covering the entire perimeter, surrounding a central vapor core. Recently, Konishi et al. [37] and Kharangate et al. [41] provided the framework for a separated flow model with those same inlet conditions, but for only single-sided heating. In the present model, which is intended for single-sided and double-sided heating, a similar framework is adopted, using slip flow assumptions, i.e., with flat velocity profiles for the individual liquid and vapor layers, but different velocities between the phases, and uniform pressure across the flow area. As shown in Fig. 8(a) and (b) for single-sided and double-sided heating, respectively, identical inlet flow patterns are assumed, with a liquid layer with uniform thickness ε_{in} surrounding a central vapor core with inlet void fraction α_{in}. This void fraction is determined by applying momentum conservation to differential control volumes of vapor and liquid of axial length Δz in the adiabatic region upstream of the heated portion of the channel, which yields the following relations,

$$G^2 \frac{d}{dz}\left[\frac{x_{e,in}^2}{\rho_g \alpha_{in}}\right] = -\alpha_{in}\frac{dp}{dz} \mp \frac{\tau_i P_i}{A} - \rho_g \alpha_{in} g_e \sin\theta \tag{1}$$

and

$$G^2 \frac{d}{dz}\left[\frac{(1-x_{e,in})^2}{\rho_f(1-\alpha_{in})}\right] = -(1-\alpha_{in})\frac{dp}{dz} - \frac{\tau_{w,f}P_{w,f}}{A} \pm \frac{\tau_i P_i}{A} \\ - \rho_f(1-\alpha_{in})g_e \sin\theta \tag{2}$$

where p, $\tau_{w,f}$, τ_i, A, $P_{w,f}$ and P_i are the pressure, wall shear stress, interfacial shear stress between the liquid and vapor layers, cross-sectional area of the channel, wall perimeter, and interfacial perimeter. The ± sign in Eq. (2) takes into account variations in shear stress direction depending on the relative velocities of the liquid and vapor layers. The inlet liquid layer thickness, ε_{in}, is related to α_{in} by the relation

$$\alpha_{in} = \frac{(H-2\varepsilon_{in})(W-2\varepsilon_{in})}{HW}. \tag{3}$$

For the heated portion of the channel, a new vapor layer is initiated along the heated wall as shown in Fig. 8(a) for single-sided heating and Fig. 8(b) for double-sided heating. The present separated flow model assumes the liquid layer continues to maintain uniform thickness, ε, on all four sides of the channel's perimeter. For single-sided heating, Fig. 8(a) shows the flow consisting of three layers: vapor layer (a) generated along the heated wall, liquid layer (c), and vapor core (d). For double-sided heating, Fig. 8(b) shows the flow consisting of four layers: vapor layer (a) along heated wall H_a, vapor layer (b) along heated wall H_b, liquid layer (c), and central vapor core (d). The model assumes the heat supplied at the wall is consumed entirely by vapor formation in layer (a) for single-sided heating, or layers (a) and (b) for double-sided heating. In other words, phase change between the liquid layer and vapor core is neglected, which is justified by the fact that these two layers enter the flow at the same saturation temperature. Therefore, the mass of the central vapor core is conserved, i.e., $x_d = x_{e,in}$. The present separated flow model deviates from the model in [41] in the treatment of the liquid layer, where only the portion of the liquid layer adjacent to the heated wall(s) was allowed to change phase. With this assumption, the previous model constrained the ability of liquid along the insulated walls from feeding the near-wall liquid and compensating for the evaporated liquid. Besides, the assumption in the previous model was observed to lead to divergence in the numerical solution. The present model is therefore modified to employ the aforementioned assumption of a circumferentially uniform liquid layer thickness.
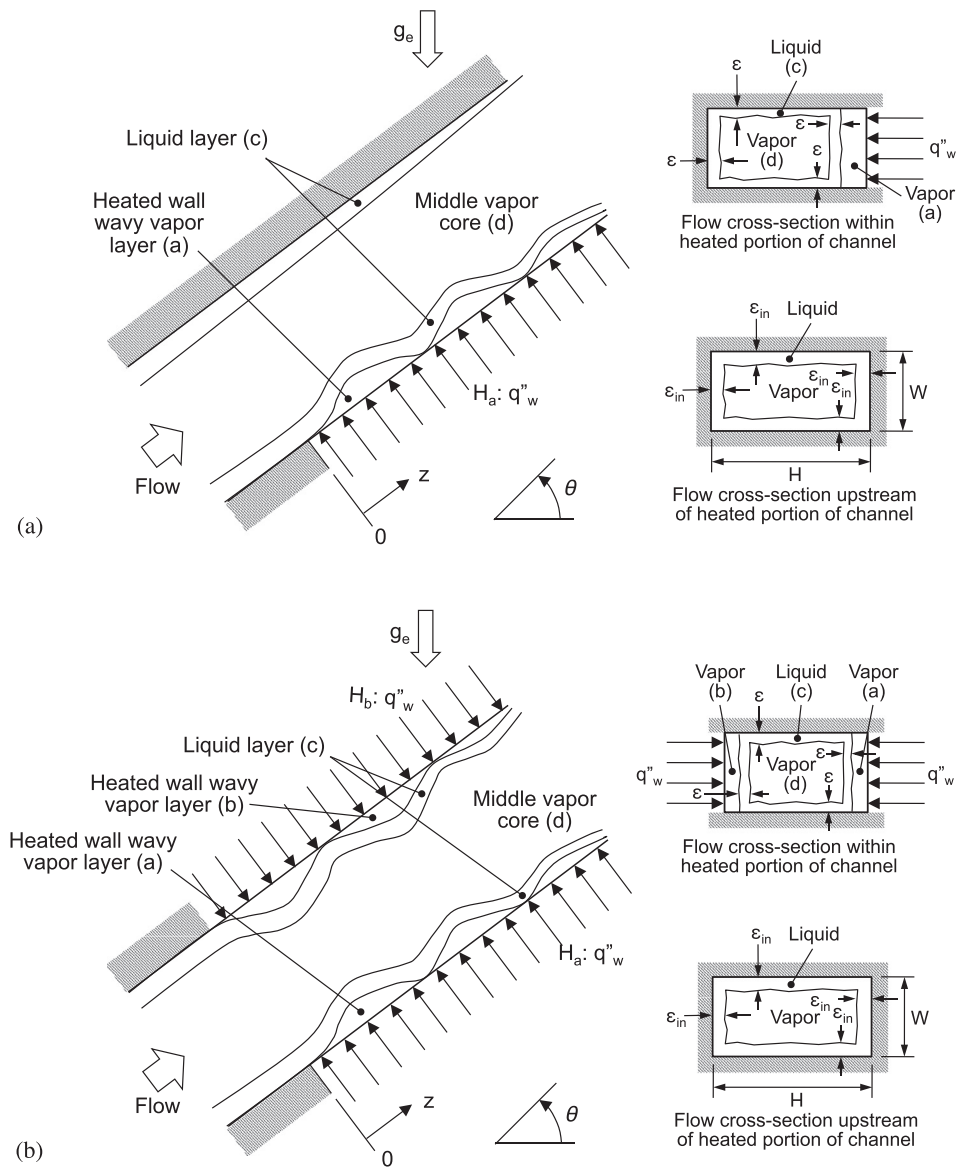
Fig. 8. Schematics of different layers in (a) single-sided heating and (b) double-sided heating configurations.

Tables 1 and 2 provide summaries of momentum and energy conservation equations for the heated portion of the channel for single-sided and double-sided heating, respectively. Table 3 provides additional relations that are used in conjunction with the conservation equations in Tables 1 and 2 to calculate key flow parameters.

Fig. 9(a)–(d) show predictions of the separated flow model for horizontal double-sided heating in Earth gravity for phase layer thicknesses, phase layer velocities, pressure, and quality, respectively, along the heated portion of the channel with $G = 800$ kg/m^2 s, $p_{in} = 150$ kPa, $x_{e,in} = 0.05$, and $q''_w = 20$ W/cm^2. Fig. 9(a) shows the vapor layers generated along the heated walls grow axially in thickness along the channel. The liquid layers are shown thinning gradually due to both loss of mass by evaporation and axially increasing shear forces. The central vapor core also grows smaller because of the increasing shear despite its mass flow rate being conserved. In the separated flow model, the liquid layer is continuous around the central vapor core, but is shown in Fig. 9(a) divided into two layers. Fig. 9(b) shows the variations of velocities of the individual layers along with velocity difference between the newly generated vapor layers and the liquid layer. The vapor core is faster than

the other layers at $z = 0$. However, the newly generated vapor layer, with velocities U_{ga} and U_{gb}, overtake the vapor core along the heated portion of the channel. The liquid layer is quickly overtaken by the two newly generated vapor layers a short distance from the leading edges of the heated walls; this trend is also reflected in the axial variation of velocity difference, ΔU, between the two vapor layers and the liquid layer. Fig. 9(c) shows the expected monotonic decrease in pressure along the heated portion of the channel. Fig. 9(d) shows thermodynamic equilibrium quality increasing axially with a constant slope because of the uniform heat supply to the two-phase mixture by the two heated walls.

4.2. Interfacial Lift-off Model

The Interfacial Lift-off Model originally proposed by Galloway and Mudawar [27,28] has been confirmed in studies spanning two decades and including CHF for short and long heated walls, flat and curved walls, horizontal, vertical, and inclined channels, and flow boiling in both Earth gravity and microgravity [15–17,29–36]. This model is also adopted here to predict the present CHF data.

Table 1
Summary of separated flow model relations for single-sided heating.

Momentum conservation:

$$G^2 \frac{d}{dz}\left[\frac{x_a^2}{\rho_g \alpha_a}\right] = -\alpha_a \frac{dp}{dz} - \frac{\tau_{w,ga}P_{w,ga}}{A} \mp \frac{\tau_{iac}P_{iac}}{A} - \rho_g \alpha_a g_e \sin\theta$$

$$G^2 \frac{d}{dz}\left[\frac{x_d^2}{\rho_g \alpha_d}\right] = -\alpha_d \frac{dp}{dz} \mp \frac{\tau_{idc}P_{idc}}{A} - \rho_g \alpha_d g_e \sin\theta$$

$$G^2 \frac{d}{dz}\left[\frac{(1-x_a-x_d)^2}{\rho_f(1-\alpha_a-\alpha_d)}\right] = -(1-\alpha_a-\alpha_d)\frac{dp}{dz} - \frac{\tau_{w,fc}P_{w,fc}}{A} \pm \frac{\tau_{iac}P_{iac}}{A} \pm \frac{\tau_{idc}P_{idc}}{A}$$
$$- \rho_f(1-\alpha_a-\alpha_d)g_e \sin\theta$$

Energy conservation:

$$\frac{dx_a}{dz} = \frac{q''_{wa}W}{\dot{m}h_{fg}}$$

$$\frac{dx_d}{dz} = 0$$

Table 2
Summary of separated flow model relations for double-sided heating.

Momentum conservation:

$$G^2 \frac{d}{dz}\left[\frac{x_a^2}{\rho_g \alpha_a}\right] = -\alpha_a \frac{dp}{dz} - \frac{\tau_{w,ga}P_{w,ga}}{A} \mp \frac{\tau_{iac}P_{iac}}{A} - \rho_g \alpha_a g_e \sin\theta$$

$$G^2 \frac{d}{dz}\left[\frac{x_b^2}{\rho_g \alpha_b}\right] = -\alpha_b \frac{dp}{dz} - \frac{\tau_{w,gb}P_{w,gb}}{A} \mp \frac{\tau_{ibc}P_{ibc}}{A} - \rho_g \alpha_b g_e \sin\theta$$

$$G^2 \frac{d}{dz}\left[\frac{x_d^2}{\rho_g \alpha_d}\right] = -\alpha_d \frac{dp}{dz} \mp \frac{\tau_{idc}P_{idc}}{A} - \rho_g \alpha_d g_e \sin\theta$$

$$G^2 \frac{d}{dz}\left[\frac{(1-x_a-x_b-x_d)^2}{\rho_f(1-\alpha_a-\alpha_b-\alpha_d)}\right] = -(1-\alpha_a-\alpha_b-\alpha_d)\frac{dp}{dz} - \frac{\tau_{w,fc}P_{w,fc}}{A} \pm \frac{\tau_{iac}P_{iac}}{A}$$
$$\pm \frac{\tau_{ibc}P_{ibc}}{A} \pm \frac{\tau_{idc}P_{idc}}{A}$$
$$- \rho_f(1-\alpha_a-\alpha_b-\alpha_d)g_e \sin\theta$$

Energy conservation:

$$\frac{dx_a}{dz} = \frac{q''_{wa}W}{\dot{m}h_{fg}}$$

$$\frac{dx_b}{dz} = \frac{q''_{wb}W}{\dot{m}h_{fg}}$$

$$\frac{dx_d}{dz} = 0$$

Table 3
Summary of relations used in conjunction with the separated flow model and Interfacial Lift-off Model.

Single-sided heating quality relations for vapor layers:

$$x_a = \frac{\rho_g U_{ga}\alpha_a}{G} \text{ and } x_d = x_{e,in}$$

Double-sided heating quality relations for vapor layers:

$$x_a = \frac{\rho_g U_{ga}\alpha_a}{G}, \ x_b = \frac{\rho_g U_{gb}\alpha_b}{G} \text{ and } x_d = x_{e,in}$$

Wall shear stress relations:

$$\tau_{w,k} = \frac{1}{2}\rho_k U_k^2 f_k$$

$$f_k = C_1 + \frac{C_2}{Re_{D_k}^{1/C_3}} = C_1 + \frac{C_2}{\left(\frac{\rho_k U_k D_k}{\mu_k}\right)^{1/C_3}}$$

where $k = fc$, ga, gb or gd. $C_1 = 0$, $C_2 = 16$ and $C_3 = 1$ for laminar flow ($Re_{D_k} \leqslant 2100$), $C_1 = 0.0054$, $C_2 = 2.3 \times 10^{-8}$ and $C_3 = -2/3$ for transitional flow ($2100 < Re_{D_k} \leqslant 4000$), and $C_1 = 0.00128$, $C_2 = 0.1143$ and $C_3 = 3.2154$ for turbulent flow ($Re_{D_k} > 4000$) [42], where $D_k = 4 A_k/P_k$

Interfacial shear stress relations:

$$\tau_{iac} = \frac{C_{f,iac}}{2}\rho_g(U_{ga}-U_{fc})^2, \ \tau_{ibc} = \frac{C_{f,ibc}}{2}\rho_g(U_{gb}-U_{fc})^2 \text{ and}$$

$$\tau_{idc} = \frac{C_{f,idc}}{2}\rho_g(U_{gd}-U_{fc})^2$$

where $C_{f,iac} = C_{f,ibc} = C_{f,idc} = 0.5$ [28]

This model is based on a detailed depiction of interfacial behavior just prior to CHF as well as the trigger event for CHF. As heat fluxes approaches CHF, a wavy vapor layer is postulated to form along the heated wall, which buffers most liquid from contacting the wall except in wetting fronts corresponding to troughs in the vapor wavy layer. Sustained boiling in the wetting fronts provides the last opportunity for cooling of the wall. The trigger event for CHF is postulated to occur as follows. The liquid contact in the wave troughs – wetting fronts – is maintained by curvature of liquid streamlines inducing a net pressure force on liquid toward the wall. This pressure force is resisted by momentum of vapor emanating within the wetting fronts normal to the wall. CHF is therefore triggered when the last increment in wall heat flux intensifies vapor momentum to a level that just exceeds the pressure force. This causes the wave trough to lift from the wall, and the wetting

front to be extinguished as a source of cooling for the wall. As a wetting front is extinguished, the heat supplied from the wall attempts to conduct heat away from this wetting front to neighboring wetting fronts. The neighboring wetting fronts now face even greater heat flux, rendering them more likely to be extinguished by lifting from the wall. Wetting fronts are therefore extinguished in succession in an unstable manner, causing the classical unsteady rise in wall temperature associated with CHF.

Flow boiling with saturated inlet conditions poses great difficulty capturing near-wall interfacial behavior by high speed video because a liquid film is formed along the channel's perimeter surrounding a central vapor core. However, the wavy vapor layer has been clearly captured in the near-wall region in the present flow visualization experiments. The main difference between the present flows with saturated inlet conditions versus subcooled inlet conditions is the existence of the vapor core for the former. The wavy vapor layer behavior for saturated inlet conditions is depicted for single-sided and double-sided heating in Fig. 10 (a) and (b), respectively, and the interfacial lift-off condition in Fig. 10(c).

As with the original Interfacial Lift-off Model [27,28], the wavy interfacial behavior is described using classical instability theory [43,44]. A sinusoidal liquid–vapor interface is assumed between the liquid layer and wall vapor layer(s), resulting from velocity differences between the two layers, gravity component acting normal to the interface, and surface tension along the interface. The wavy interface is described by the perturbation function $\eta(z,t) = \eta_0 e^{ik_m(z-c_m t)}$, where η_0 is the wave amplitude, k_m the wave number, and c_m the wave speed. The wave speed is expressed $c_m = c_{r,m} + i\ c_{i,m}$, where $c_{r,m}$ and $c_{i,m}$ are real and imaginary components, respectively. As shown in Fig. 10(a) and (b), the real component defines the actual propagation speed of the interface, while the imaginary component is associated with amplification or decay of the interfacial perturbation.

The interfacial instability model yields the following relation for the imaginary component,

$$c_{i,m} = \sqrt{\frac{\rho_f'' \rho_{gm}''(U_{gm} - U_f)^2}{(\rho_f'' + \rho_{gm}'')^2} + \frac{(\rho_f - \rho_{gm}) g_{nm}}{(\rho_f'' + \rho_{gm}'')} \frac{g_{nm}}{k_m} - \frac{\sigma k_m}{(\rho_f'' + \rho_{gm}'')}}, \quad (4)$$

where ρ_f'' and ρ_{gm}'' are modified density terms. The interface is deemed stable when $c_{i,m} < 0$, implying the interfacial perturbation will decay with time, which would prevent the formation of wetting fronts. On the other hand, the interface is rendered unstable when $c_{i,m} > 0$, meaning the perturbation would amplify, allowing wetting fronts to form along the wall. The onset of interfacial stability corresponding to $c_{i,m} = 0$ constitutes the minimum requirement for the perturbation to begin forming wetting fronts, and is therefore used in the Interfacial Lift-off Model to determine interfacial wavelength. Setting $c_{i,m}$ given by Eq. (4) equal to zero yields the following relation for critical wave number, $k_{c,m}$, and critical wavelength, $\lambda_{c,m}$,

$$k_{c,m} = \frac{2\pi}{\lambda_{c,m}} = \frac{\rho_f'' \rho_{gm}''(U_{gm} - U_f)^2}{2\sigma(\rho_f'' + \rho_{gm}'')}$$
$$+ \sqrt{\left[\frac{\rho_f'' \rho_{gm}''(U_{gm} - U_f)^2}{2\sigma(\rho_f'' + \rho_{gm}'')}\right]^2 + \frac{(\rho_f - \rho_{gm})g_{nm}}{\sigma}}, \quad (5)$$

where $\rho_f'' = \rho_f \coth(2\pi\varepsilon/\lambda_{c,m})$ and $\rho_{gm}'' = \rho_g \coth(2\pi\delta_m/\lambda_{c,m})$. Eq. (5) is used to determine critical wavelengths for both single-sided and double-sided heating. For double-sided heating, however, critical wavelengths are different for the two opposite heated walls because of opposite directions of gravity components perpendicular to these walls. In Earth gravity, the gravity components normal to

the upward-facing heated wall and downward-facing heated wall are expressed, respectively, as

$$g_{na} = g_e \cos\theta \quad (6a)$$

and

$$g_{nb} = g_e \cos(\theta + \pi) = -g_e \cos\theta \quad (6b)$$

According to the Interfacial Lift-off Model, based on extensive evidence from flow visualization experiments, a continuous wetting front region of axial length z_m^* is formed along the leading edge of the heated wall, which is given by

$$z_m^* = z_{0,m} + \lambda_{c,m}(z_m^*) \quad (7)$$

where z_0 is the distance from the leading edge to the axial location where heated wall vapor layer velocity just exceeds liquid layer velocity. Fig. 9(b) shows $z_0 = 2$ mm for horizontal double-sided heating in Earth gravity for FC-72 with $G = 800$ kg/m^2 s, $p_{in} = 150$ kPa, $x_{e,in} = 0.05$, and $q_w'' = 20$ W/cm^2. Zhang et al. [35] statistically analyzed video segments captured just prior to CHF, and showed that waves generated at z_m^* have a tendency to preserve curvature as they propagate downstream. Therefore, in the present study, the curvatures of waves at CHF anywhere along the heated wall are assumed identical to that at z_m^*.
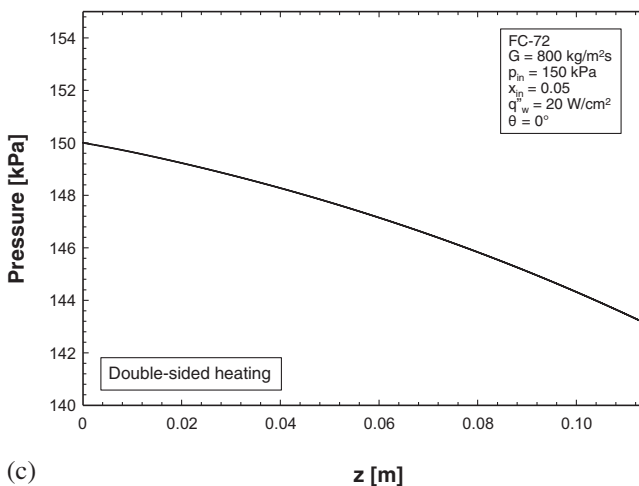
Illustrated in Fig. 10(c) is the trigger event for CHF according to the Interfacial Lift-off Model, where the normal momentum of vapor generated in the wetting front just exceeds the pressure force induced by streamline curvature that pushes the interface
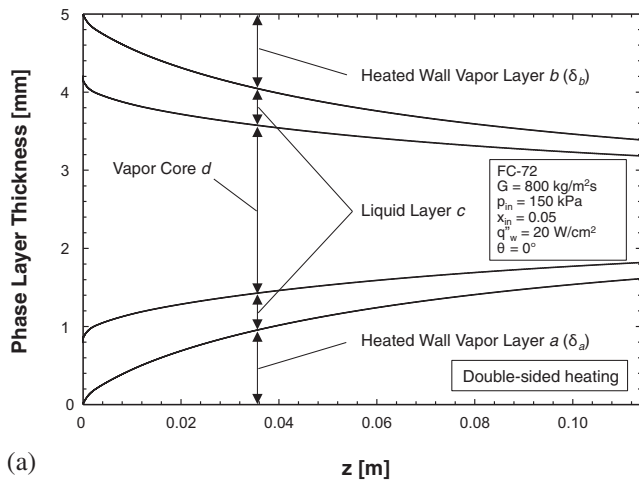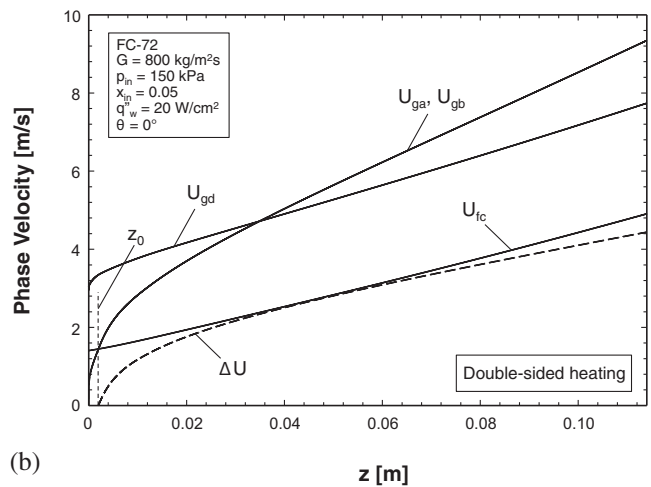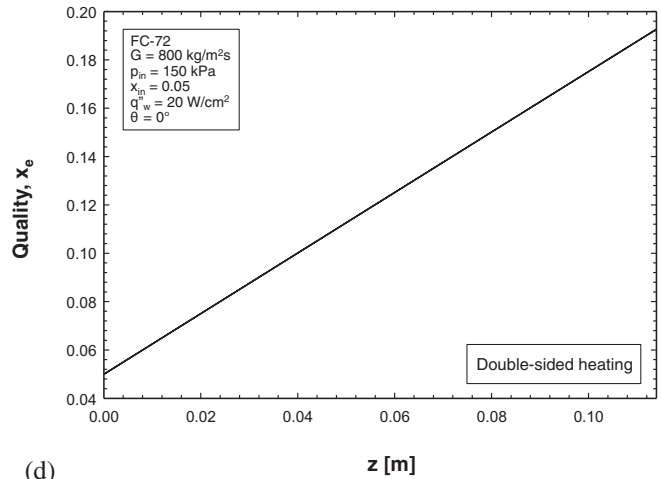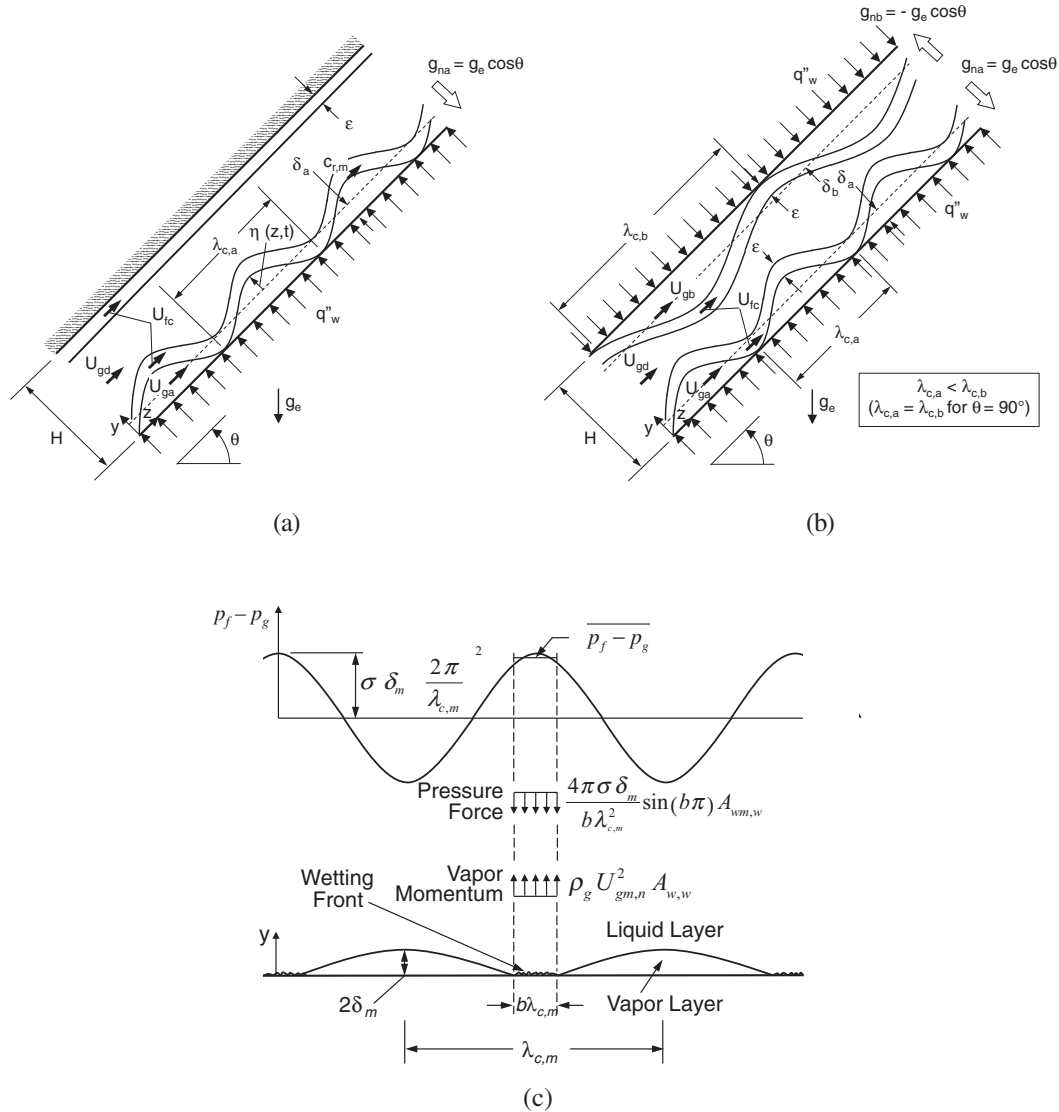

Fig. 9. Separated flow model predictions of (a) phase layer thicknesses, (b) phase velocities, (c) pressure, and (d) quality.

Fig. 10. Hydrodynamic instability of wavy vapor layers along heated walls for inclined channel just before CHF for (a) single-sided heating and (b) double-sided heating configurations. (c) Schematic representation of interfacial lift-off from heated wall in wetting front at CHF.

toward the heated wall. Zhang et al. [45] showed that the average pressure difference at the wetting front is given by

$$\overline{p_f - p_g} = \frac{4\pi\sigma\delta_m}{b\lambda_{c,m}^2} \sin(b\pi). \tag{8}$$

With the fluid entering the channel as a two-phase mixture, the heat flux, $q''_{w,w}$, required to convert saturated liquid to saturated vapor for incoming liquid in the wetting front can be expressed as

$$q''_{wm,w}A_{wm,w} = \rho_g U_{gm,n}A_{wm,w}[h_{fg}(1 - x_{e,in})], \tag{9}$$

where $A_{wm,w}$ is the wetting front's area and $U_{gm,n}$ the velocity of vapor normal to the heated wall. Equating the normal vapor momentum, $\rho_g U_{gm,n}^2$, to the average pressure difference acting on the interface in the wetting front, Eq. (8), and substituting into Eq. (9), yield the following relation for lift-off heat flux in the wetting front,

$$q''_{wm,w} = \rho_g\left[h_{fg}(1 - x_{e,n})\right]\sqrt{\frac{\overline{p_f - p_g}}{\rho_g}} = \rho_g[h_{fg}(1 - x_{e,n})]\left[\frac{4\pi\sigma}{\rho_g}\frac{\sin(b\pi)}{b}\right]^{1/2}\frac{\delta_m^{1/2}}{\lambda_{c,m}}. \tag{10}$$

High speed video analysis of near-wall interfacial behavior by Sturgis and Mudawar [32,33] showed that the wetting front maintains an axial length as a fixed fraction $b = 0.20$ of the local wavelength. As liquid is converted to vapor only in the wetting fronts, CHF is calculated by multiplying the wetting front's lift-off heat flux by this fraction,

$$CHF_{pred,m} = bq''_{wm,w}. \tag{11}$$

Combining Eqs. (10) and (11) yields the following analytical expression for CHF,

$$CHF_{pred,m} = \rho_g[h_{fg}(1 - x_{e,in})]\left[\frac{4\pi\sigma b\sin(b\pi)}{\rho_g}\right]^{1/2}\frac{\delta_m^{1/2}}{\lambda_{c,m}}\bigg|_{z^*}. \tag{12}$$

For double-sided heating, CHF is calculated for both upward-facing and downward facing walls separately. Then, CHF for a test case is chosen as the minimum of the two predicted CHF values,

$$CHF_{pred} = \min(CHF_{pred,a}, CHF_{pred,b}). \tag{13}$$

4.3. CHF model predictions

Before comparing CHF data to predictions of the Interfacial Lift-off Model, it is important to identify the range of operating conditions associated with formation of a wavy vapor layer. For subcooled inlet conditions, Kharangate et al. [38] showed that CHF for an upward-facing heated wall yields interfacial behavior resembling that of pool boiling rather than exhibiting a wavy vapor layer for $G < 800$ kg/m^2 s. They also observed a vapor layer with a stable interface for a downward-facing heated wall for $G < 800$ kg/m^2 s. Additionally, the flow visualization results discussed earlier in the present study prove that the interfacial behavior for certain orientations is entirely gravity dominated for $G \leqslant 400$ kg/m^2 s. Therefore, in the present study, only CHF data corresponding to $G \geqslant 800$ kg/m^2 s are compared to predictions of the interfacial Lift-off Model.

Fig. 11(a)–(c) compare variations of CHF predictions and CHF data for single-sided heating with orientation for different mass velocities, and inlet qualities of $x_{e,in} = 0.00$–0.04, 0.07–0.13, and 0.19–0.22, respectively. For $G = 790.7$–863.6 kg/m^2 s and $x_{e,in} = 0.03$–0.04, Fig. 11(a) shows both predicted and measured CHF are highest for $\theta = 0°$ and lowest for combinations of downflow and downward-facing heated wall orientations ($\theta = 180°$ to $\theta = 270°$). At higher mass velocities, the CHF data do not exhibit significant variations with orientation, yet the model predictions still

follow the trends for $G = 790.7$–863.6 kg/m^2 s. The highest discrepancy between predictions and experiment at the lowest mass velocity of $G = 790.7$–863.6 kg/m^2 s are encountered at $\theta = 180°$. As stated earlier, the Interfacial Lift-off Model is applied only to CHF data corresponding to $G \geqslant 800$ kg/m^2 s. The model is not applicable to the transition mass velocity range with the lowest inlet quality for this orientation, where gravity effects are quite significant. As inlet quality is increased, Fig. 11(b) and (c), the model predictions improve in both magnitude and trend, excepting the orientation $\theta = 0°$ in Fig. 11(b). Fig. 11(d) compares the predictions of the Interfacial Lift-off Model with CHF data for single-sided heating for $G \geqslant 800$ kg/m^2 s. The predictive accuracy of the model is assessed using mean absolute error (MEA), which is defined as

$$MAE = \frac{1}{N} \sum \left| \frac{CHF_{pred} - CHF_{exp}}{CHF_{exp}} \right| \tag{14}$$

Overall, vertical upflow ($\theta = 90°$) and vertical downflow ($\theta = 270°$) show the best agreement, with MAEs of 5.8% and 4.7%, respectively, and horizontal upward-facing heated wall ($\theta = 0°$) and horizontal downward-facing heated wall ($\theta = 180°$) showing slightly higher MAEs of 14.0% and 10.4%, respectively.

Fig. 12(a)–(c) compare variations of CHF predictions and CHF data for double-sided heating with orientation for different mass velocities, and inlet qualities of $x_{e,in} = 0.00$–0.04, 0.06–0.12, and 0.18–0.22, respectively. For the lowest $x_{e,in}$ range, Fig. 12(a) shows
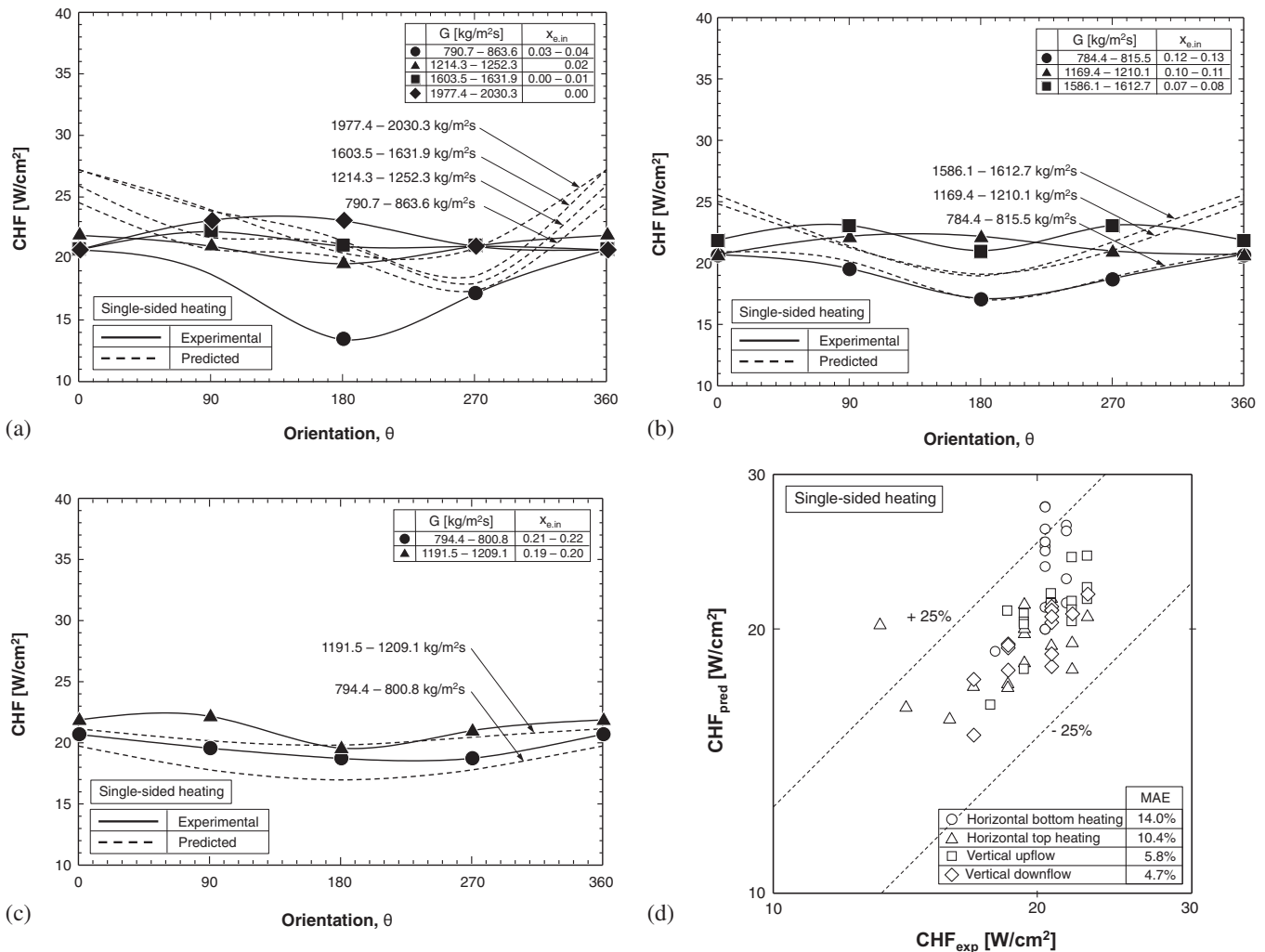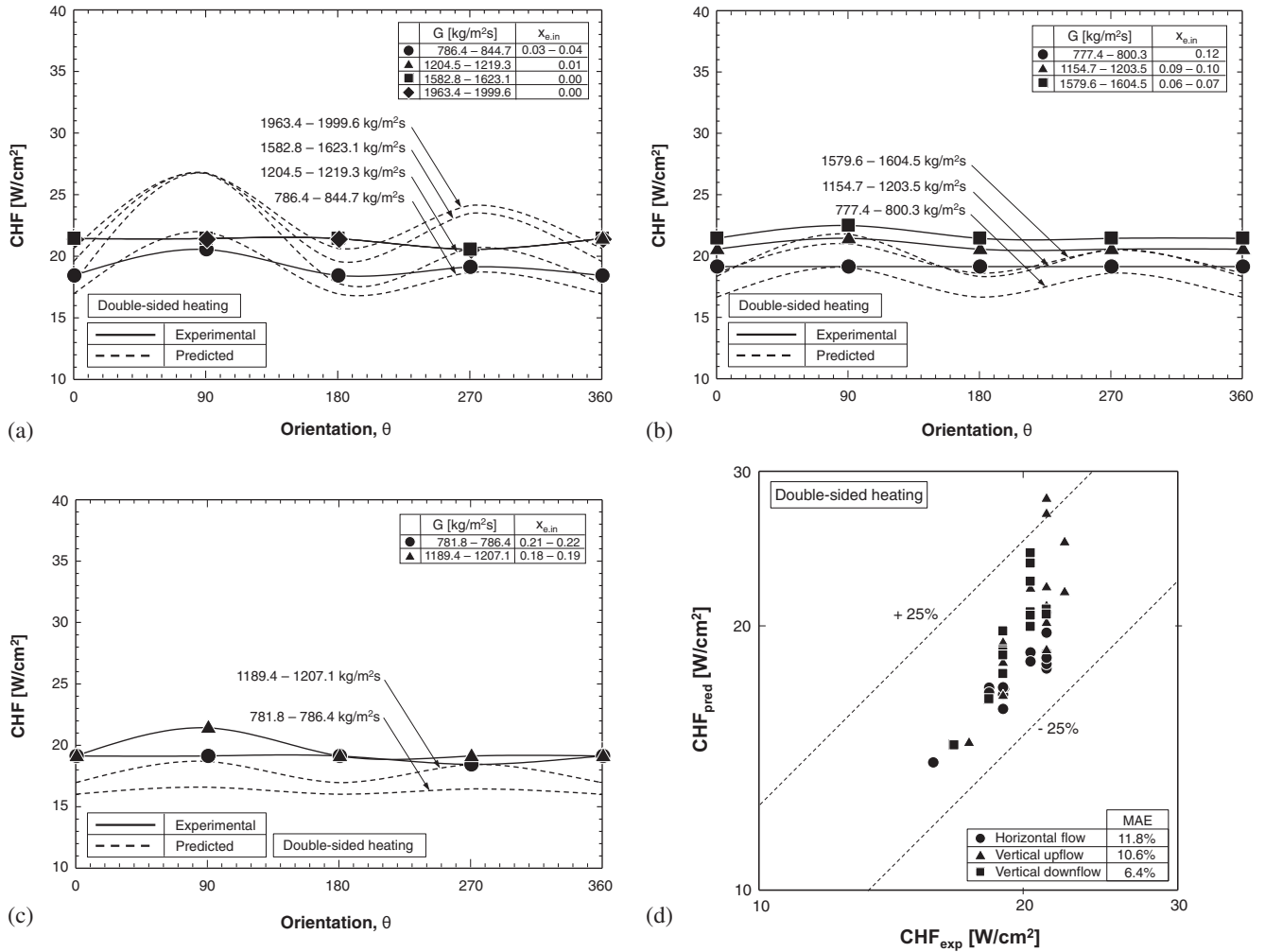

Fig. 11. Comparison of measured and predicted CHF with single-sided heating for (a) $x_{e,in} = 0.00$–0.04, (b) $x_{e,in} = 0.07$–0.13, and (c) $x_{e,in} = 0.19$–0.22. (d) Predicted versus measured CHF for all test cases with single-sided heating.

Fig. 12. Comparison of measured and predicted CHF with double-sided heating for (a) $x_{e,in}$ = 0.00–0.04, (b) $x_{e,in}$ = 0.06–0.12, and (c) $x_{e,in}$ = 0.18–0.22. (d) Predicted versus measured CHF for all test cases with double-sided heating.

peak predicted CHF values for vertical upflow ($\theta = 90°$), followed by vertical downflow ($\theta = 270°$), and minimum values for horizontal flows ($\theta = 0°$ and $180°$). While the model does capture the data trends in Fig. 12(a), it predicts a stronger orientation influence. However, the model shows better agreement with the data for the two higher quality ranges, Fig. 12(b) and (c). Fig. 12(d) compares predictions of the Interfacial Lift-off Model with CHF data for double-sided heating for $G \geqslant 800$ kg/m² s. The model shows good overall predictions, with MAEs for horizontal flows ($\theta = 0°$ and $180°$), vertical upflow ($\theta = 90°$), and vertical downflow ($\theta = 270°$) of 11.8%, 10.6% and 6.4%, respectively.

These results demonstrate that the combination of separated flow model and Interfacial Lift-off Model is as effective at predicting CHF for saturated inlet conditions as it is for subcooled inlet conditions in many prior studies [15–17,29–36]. In fact, the model shows better predictive accuracy for both single-sided and double-sided heating with higher inlet qualities than with lower qualities or subcooled inlet conditions.

5. Conclusions

This second part of a two-part study explored flow boiling critical heat flux (CHF) of FC-72 along a rectangular channel with either one wall or two opposite walls heated for saturated inlet conditions. The first part of the study examined flow boiling inter-

facial behavior, boiling curves, local and average heat transfer coefficients, and pressure drops. This part was focused entirely on CHF measurement, flow visualization and modeling. Key finding from this part are as follows:

(1) Flow visualization of CHF showed that gravity plays a dominant role for $G \leqslant 400$ kg/m² s. For horizontal orientations, top wall heating, and top and bottom wall heating show wetting fronts being lifted away from heated wall(s) during CHF for lower qualities and lower mass velocities. Interfacial behavior along the bottom wall is difficult to observe due to the vapor generated along the heated wall combining with vapor entering the flow channel. For vertical orientations, a turbulent vapor–liquid mixture is observed engulfing the walls during CHF.

(2) For low mass velocities and single sided-heating, lowest CHF values are achieved for top-wall heating ($\theta = 180°$) due to vapor stratification along the heated wall, and highest for bottom-wall heating ($\theta = 0°$), due to strong buoyancy effects aiding vapor removal from, and liquid replenishment of the heated wall in the latter. For low mass velocities and double sided-heating, horizontal orientations yield lower CHF values compared to both vertical upflow and downflow because of inferior performance of the top heated wall in horizontal flow.

(3) For both single-sided heating and double-sided heating, mass velocity decreases the influence of orientation on CHF, with identical CHF values achieved at high mass velocities irrespective of orientation. Also, increasing inlet quality serves to decrease the mass velocity required for inertia to negate gravity effects.

(4) With an overall MAE ⩽ 14%, this study shows that the combination of separated flow model and *Interfacial Lift-off Model* is very effective at predicting CHF for saturated inlet conditions as it did for subcooled inlet conditions in prior studies. Increasing inlet quality improves CHF predictions for both single-sided and double-sided heating.

Acknowledgements

References

[1] I. Mudawar, Two-phase micro-channel heat sinks: theory, applications and limitations, J. Electron. Packag. 133 (2011) 041002.

[2] F.P. Chiaramonte, J.A. Joshi, Workshop on critical issues in microgravity fluids, transport, and reaction processes in advanced human support technology – final report, NASA TM-2004-212940, 2004.

[3] I. Mudawar, T.M. Anderson, Optimization of extended surfaces for high flux chip cooling by pool boiling, J. Electron. Packag. 115 (1993) 89–100.

[4] P.J. Marto, V.J. Lepere, Pool boiling heat transfer from enhanced surfaces to dielectric fluids, J. Heat Transfer 104 (1982) 292–299.

[5] S. Mukherjee, I. Mudawar, Smart pumpless loop for micro-channel electronic cooling using flat and enhanced surfaces, IEEE Trans. CPMT 26 (2003) 99–109.

[6] J.A. Shmerler, I. Mudawar, Local evaporative heat transfer coefficient in turbulent free-falling liquid films, Int. J. Heat Mass Transfer 31 (1988) 731–742.

[7] T.H. Lyu, I. Mudawar, Statistical investigation of the relationship between interfacial waviness and sensible heat transfer to a falling liquid film, Int. J. Heat Mass Transfer 34 (1991) 1451–1464.

[8] K.E. Gungor, R.H.S. Winterton, General correlation for flow boiling in tubes and annuli, Int. J. Heat Mass Transfer 29 (1986) 351–358.

[9] H.J. Lee, S.Y. Lee, Heat transfer correlation for boiling flows in small rectangular horizontal channels with low aspect ratios, Int. J. Multiphase Flow 27 (2001) 2043–2062.

[10] M. Monde, T. Inoue, Critical heat flux in saturated forced convective boiling on a heated disk with multiple impinging jets, J. Heat Transfer 113 (1991) 722–727.

[11] M.E. Johns, I. Mudawar, An ultra-high power two-phase jet-impingement avionic clamshell module, J. Electron. Packag. 118 (1996) 264–270.

[12] D.D. Hall, I. Mudawar, Experimental and numerical study of quenching complex-shaped metallic alloys with multiple, overlapping sprays, Int. J. Heat Mass Transfer 38 (1995) 1201–1216.

[13] L. Lin, R. Ponnappan, Heat transfer characteristics of spray cooling in a closed loop, Int. J. Heat Mass Transfer 46 (2003) 3737–3746.

[14] M. Visaria, I. Mudawar, Theoretical and experimental study of the effects of spray orientation on two-phase spray cooling and critical heat flux, Int. J. Heat Mass Transfer 51 (2008) 2398–2410.

[15] J.C. Sturgis, I. Mudawar, Critical heat flux in a long, curved channel subjected to concave heating, Int. J. Heat Mass Transfer 42 (1999) 3831–3848.

[16] J.C. Sturgis, I. Mudawar, Assessment of CHF enhancement mechanisms in a curved, rectangular channel subjected to concave heating, J. Heat Transfer 121 (1999) 394–404.

[17] J.E. Galloway, I. Mudawar, Critical heat flux enhancement by means of liquid subcooling and centrifugal force induced by flow curvature, Int. J. Heat Mass Transfer 35 (1992) 1247–1260.

[18] C. Konishi, I. Mudawar, Review of flow boiling and critical heat flux in microgravity, Int. J. Heat Mass Transfer 80 (2015) 469–493.

[19] Y. Katto, H. Ohno, An improved version of the generalized correlation of critical heat flux for the forced convective boiling in uniformly heated vertical tubes, Int. J. Heat Mass Transfer 27 (1984) 1641–1648.

[20] D.C. Groeneveld, L.K.H. Leung, P.L. Kirillov, V.P. Bobkov, I.P. Smogalev, V.N. Vinogradov, X.C. Huang, E. Royer, The look-up table for critical heat flux in tubes, Nucl. Eng. Des. 163 (1996) 1–23.

[21] D.D. Hall, I. Mudawar, Critical heat flux (CHF) for water flow in tubes – I. Compilation and assessment of world CHF data, Int. J. Heat Mass Transfer 43 (2000) 2573–2604.

[22] D.D. Hall, I. Mudawar, Critical heat flux (CHF) for water flow in tubes – II. Subcooled CHF correlations, Int. J. Heat Mass Transfer 43 (2000) 2605–2640.

[23] S.S. Kutateladze, A.I. Leont'ev, Some applications of the asymptotic theory of the turbulent boundary layer, in: Proc. 3rd Int. Heat Transfer Conf., vol. 3, 1966, pp. 1–6 (Chicago, Illinois).

[24] J. Weisman, B.S. Pei, Prediction of critical heat flux in flow boiling at low qualities, Int. J. Heat Mass Transfer 26 (1983) 1463–1477.

[25] C.H. Lee, I. Mudawar, A mechanistic critical heat flux model for subcooled flow boiling based on local bulk flow conditions, Int. J. Multiphase Flow 14 (1988) 711–728.

[26] G.P. Celata, M. Cumo, Y. Katto, A. Mariani, Prediction of the critical heat flux in water subcooled flow boiling using a new mechanistic approach, Int. J. Heat Mass Transfer 42 (1999) 1457–1466.

[27] J.E. Galloway, I. Mudawar, CHF mechanism in flow boiling from a short heated wall-part 1. Examination of near-wall conditions with the aid of photomicrography and high-speed video imaging, Int. J. Heat Mass Transfer 36 (1993) 2511–2526.

[28] J.E. Galloway, I. Mudawar, CHF mechanism in flow boiling from a short heated wall-part 2. Theoretical CHF model, Int. J. Heat Mass Transfer 36 (1993) 2527–2540.

[29] J.E. Galloway, I. Mudawar, A theoretical model for flow boiling CHF from concave heaters, J. Heat Transfer 117 (1995) 698–707.

[30] C.O. Gersey, I. Mudawar, Effects of heater length and orientation on the trigger mechanism for near-saturated flow boiling CHF – I. Photographic and statistical characterization of the near-wall interfacial features, Int. J. Heat Mass Transfer 38 (1995) 629–642.

[31] C.O. Gersey, I. Mudawar, Effects of heater length and orientation on the trigger mechanism for near-saturated flow boiling CHF – II. CHF model, Int. J. Heat Mass Transfer 38 (1995) 643–654.

[32] J.C. Sturgis, I. Mudawar, Critical heat flux in a long, rectangular channel subjected to one-sided heating – I. Flow visualization, Int. J. Heat Mass Transfer 42 (1999) 1835–1847.

[33] J.C. Sturgis, I. Mudawar, Critical heat flux in a long, rectangular channel subjected to one-sided heating – II. Analysis of CHF data, Int. J. Heat Mass Transfer 42 (1999) 1849–1862.

[34] H. Zhang, I. Mudawar, M.M. Hasan, Experimental assessment of the effects of body force, surface tension force, and inertia on flow boiling CHF, Int. J. Heat Mass Transfer 45 (2002) 4079–4095.

[35] H. Zhang, I. Mudawar, M.M. Hasan, Experimental and theoretical study of orientation on flow boiling CHF, Int. J. Heat Mass Transfer 45 (2002) 4463–4477.

[36] H. Zhang, I. Mudawar, M.M. Hasan, Flow boiling CHF in microgravity, Int. J. Heat Mass Transfer 48 (2005) 3107–3118.

[37] C. Konishi, I. Mudawar, Investigation of the influence of orientation on critical heat flux for flow boiling with two-phase inlet, Int. J. Heat Mass Transfer 61 (2013) 176–190.

[38] C.R. Kharangate, L. O'Neill, I. Mudawar, M.M. Hasan, H.K. Nahra, R. Balasubramaniam, N.R. Hall, A.M. Macner, J.R. Mackey, Effects of subcooling and two-phase inlet on flow boiling heat transfer and critical heat flux in a horizontal channel with one-sided and double-sided heating, Int. J. Heat Mass Transfer 91 (2015) 1187–1205.

[39] C.R. Kharangate, L. O'Neill, I. Mudawar, M.M. Hasan, H.K. Nahra, R. Balasubramaniam, N.R. Hall, A.M. Macner, J.R. Mackey, Flow boiling and critical heat flux in horizontal channel with one-sided and double-sided heating, Int. J. Heat Mass Transfer 90 (2015) 323–338.

[40] C.R. Kharangate, L. O'Neill, I. Mudawar, Effects of two-phase inlet quality, mass velocity, flow orientation, and heating perimeter on flow boiling in a rectangular channel: Part 1 – Two-phase flow and heat transfer results, Int. J. Heat Mass Transfer 103 (2016) 1261–1279.

[41] C.R. Kharangate, I. Mudawar, M.M. Hasan, Experimental and theoretical study of critical heat flux in vertical upflow with inlet vapor void, Int. J. Heat Mass Transfer 55 (2012) 360–374.

[42] M.S. Bhatti, R.K. Shah, Turbulent and transitional convective heat transfer in ducts, in: S. Kakac, R.K. Shah, W. Aung (Eds.), Handbook of Single-phase Convective Heat Transfer, John Wiley and Sons, NY, 1987.

[43] H. Lamb, Hydrodynamics, sixth ed., Dover Publications, NY, 1945.

[44] L.M. Milne-Thompson, Theoretical Hydrodynamics, fourth ed., Macmillan, NY, 1960.

[45] H. Zhang, I. Mudawar, M.M. Hasan, CHF model for subcooled flow boiling in Earth gravity and microgravity, Int. J. Heat Mass Transfer 50 (2007) 4039–4051.